journal of physics

Vol. 50 No. 3
March 1998

AN ACADEMY OF SCIENCES

Associate Editor

H R Krishnamurthy
Indian Institute of Science, Bangalore

Editorial Board

G S Agarwal, *Physical Research Laboratory, Ahmedabad*
V Balakrishnan, *Indian Institute of Technology, Chennai*
J K Bhattacharjee, *Indian Assoc. for the Cultivation of Science, Calcutta*
D N Bose, *Indian Institute of Technology, Kharagpur*
B M Deb, *Panjab University, Chandigarh*
Rohini M Godbole, *Indian Institute of Science, Bangalore*
S Kailas, *Bhabha Atomic Research Centre, Mumbai*
R K Kaul, *The Institute of Mathematical Sciences, Chennai*
A V Khare, *Institute of Physics, Bhubaneswar*
T Padmanabhan, *Inter-Univ. Centre for Astronomy and Astrophysics, Pune*
R Ramaswamy, *Jawaharlal Nehru University, New Delhi*
A K Raychaudhuri, *National Physical Laboratory, New Delhi*
K C Rustagi, *Centre for Advanced Technology, Indore*
E V Sampathkumaran, *Tata Institute of Fundamental Research, Mumbai*
Abhijit Sen, *Institute for Plasma Research, Gandhinagar*
S K Sikka, *Bhabha Atomic Research Centre, Mumbai*
Y Singh, *Banaras Hindu University, Varanasi*

Editor of Publications of the Academy

N Mukunda
Indian Institute of Science, Bangalore

Annual Subscription Rates

All countries except India (Price includes AIR MAIL charges)	US$ 200
India	Rs. 200

Annual subscriptions for individuals for India and abroad are Rs. 100/- and $50 respectively.

All correspondence regarding subscription should be addressed to the Circulation Department of the Academy

---

Editorial Office

Indian Academy of Sciences, C V Raman Avenue,
P.B. No. 8005, Bangalore 560 080, India

Telephone: 334 2546
Telefax: 91-80-334 6094

Email: pramana@ias.ernet.in

A computer simulation study of ionic conductivity in polymer electrolytes

ANINDA JIBAN BHATTACHARYYA, T R MIDDYA and S TARAFDAR
Department of Physics, Condensed Matter Physics Research Center, Jadavpur University, Calcutta 700 032, India
Email: aninda@juphys.ernet.in

Abstract. In this paper we present a computer simulation study of ionic conductivity in solid polymeric electrolytes. The multiphase nature of the material is taken into account. The polymer is represented by a regular lattice whose sites represent either crystalline or amorphous regions with the charge carrier performing a random walk. Different waiting times are assigned to sites corresponding to the different phases. A random walk (RW) is used to calculate the conductivity through the Nernst–Einstein relation. Our walk algorithm takes into account the reorganization of the different phases over time scales comparable to time scales for the conduction process. This is a characteristic feature of the polymer network. The qualitative nature of the variation of conductivity with salt concentration agrees with the experimental values for PEO–NH_4I and PEO–NH_4SCN. The average jump distance estimated from our work is consistent with the reported bond lengths for such polymers.

Keywords. Polymer electrolytes; ionic conductivity; random walk; computer simulation.

PACS Nos 66.30; 61.43; 61.41

1. Introduction

During the last two decades a lot of interest has been generated in the potential industrial applications of polymer electrolytes [1, 2]. Hence, developement of theoretical understanding of such materials is essential. Polymeric solid electrolytes are formed by complexing an ionic salt like NaI, NH_4SCN, etc with polymers, for example polyethylene oxide (PEO), polypropylene oxide (PPO), [3, 4] etc. We restrict our discussion to solvent free polymer electrolytes which are formed by dissolving or suspending the salt and the polymer in a suitable solvent and then evaporating the solvent during casting.

The theoretical explanation of the dependence of ionic transport on temperature, salt fraction, frequency, etc. is a formidable problem. The complications arise mainly because these polymer systems are multiphase in nature. Further difficulties creep in because the presence of different phases are dependent on processing conditions and thermal history.

The aim of this work is to study the variation of ionic conductivity in a polymer electrolyte where the salt fraction is varied. The varying salt fraction changes the proportion of crystalline and amorphous regions and also the concentration of charge carriers supplied by the salt [5].

computer simulation of a random walk (RW) [6–8]. Appropriate algorithms to represent phases of different conductivity may be incorporated into such models. Often a continuous time random walk (CTRW) [8] is used. A recent work [9] introduces a method for speeding up a CTRW calculation by a modified blind ant algorithm which makes the walker jump at every step but adjusts the time to account for the waiting time.

The dynamic bond percolation model by Druger *et al* [10, 11] is used to calculate the conductivity of a polymer through computer simulation of a hopping model. This model incorporates the dynamic nature of the medium by introducing a renewal time. The frequency dependence of the conductivity within a certain range can be explained by this model. The model fails however at the very high frequency limit, since inertial effects are not taken into account.

2. The model

In the present paper our main aim is to develop an algorithm utilizing some experimental inputs to explain the salt fraction dependence of ionic conductivity of polymer-salt systems. The solvent free polymer electrolytes are prepared in the form of thin films. Hence, as a preliminary approximation, in this paper we consider the polymer electrolyte as a two dimensional space lattice. Rather than dealing with bonds, our model deals with sites only. A random walk is executed on the square lattice. The uniform square lattice does not of course represent the structure of the polymer network which is disordered, but only provides a convenient space for executing the random walk.

We designate a site on the lattice as amorphous or crystalline. The sites actually represent very small regions of the polymer complex which belong to a single phase only, and the lattice spacing (ξ) represents the distance between such sites. We assign a jump probability to each site representing the conductivity of the phase to which the site belongs.

However, our model is not a 'quenched' model. The walker sees a site as crystalline or amorphous statistically according to a random number chosen on its visit to the site. The probability of the site being, say crystalline, is determined from the experimental crystallinity. This means that a site previously found to be crystalline may become amorphous on a later visit. A crystalline site may also become amorphous or vice versa, during the waiting time of the walker at that site.

This procedure is often adopted to make the walk algorithm simpler and provide an effectively infinite system. Here however, it gives an added advantage. The polymer, as distinct from crystalline or glassy superionic conductors is known to show a dynamic disorder, i.e. the matrix is continually rearranging itself after a characteristic (renewal) time τ_r. The RW algorithm thus gives a more realistic picture of the polymer, though in from experimental estimates of crystallinity from differential thermal analysis (DTA) or x-ray diffraction (XRD), and the distribution of these phases in the lattice is random. A site belonging to the ith phase is assigned a jump probability p_i for jumping to a nearest neighbour site, at each time step. The time elapsed (inverse of p_i) between arrival at one site and arrival at the next site includes τ_j the time taken to jump from one site to a nearest neighbour and an average waiting time $\langle \tau_i \rangle$ at the ith site. A longer waiting time corresponds to a lower conductivity of the phase and hence of the site. In the present case we have two waiting times, τ_{a} for the amorphous phase and τ_{c} for the crystalline phase which is larger.

A distribution of energetically different sites on a lattice is usually represented in a simulation model by either of the following pictures:

(a) A well model, where each site is a potential well. Here the well depth w_i is characteristic of that particular site i, and determines how long the random walker will be trapped there.
(b) A barrier model where a barrier of height h_{ij}, is envisaged between the sites i and j. Here the probability of hopping to i from j may be determined by the nature of both the sites i and j.

In the present work we employ the considerably simpler well model, where the probability of leaving a site is determined by the phase of this site, but the carrier has an equal probability of going to all four nearest neighbours whether they are crystalline or amorphous. In view of the dynamic disorder, where the polymer chains can reorient within the time interval τ, which the random walker takes to hop to a neighbouring site, model (a) seems quite adequate.

In case of normal diffusion, the diffusion coefficient can be obtained from a random walk, through the relation

$$\langle r^2(t) \rangle = 2dDt, \tag{1}$$

where $\langle r^2 \rangle$ is the average square distance covered by the walker in t time steps and d is the dimension of the space lattice. The constant D is the diffusion coefficient.

In real units the diffusion coefficient is given by

$$D = \frac{\langle r^2 \rangle}{4t} \frac{(\text{distance unit})^2}{(\text{time unit})}. \tag{2}$$

The distance unit = the lattice constant (ξ) and time unit = τ, the time step. In our model $\tau = \tau_j$ the time taken in jumping from one site to another, waiting time at a site is measured in units of τ. The steps of the RW are given below

1. The walker is released at a randomly chosen site on a two dimensional lattice.

the walker jumps to the left neighbour. If

$$\frac{p_i}{4} < R_2 \leq \frac{p_i}{2},$$

the walker jumps to the right neighbour. If

$$\frac{p_i}{2} < R_2 \leq \frac{3p_i}{4},$$

the walker moves to the upper neighbour and if

$$\frac{3p_i}{4} < R_2 \leq p_i,$$

the walker moves to the lower neighbour. If

$$p_i < R_2 \leq 1,$$

it does not jump at all.

In case the walker has jumped, it again checks whether the new site is crystalline or amorphous by step (2). Even if it has not jumped, step (2) is repeated to account for the reorganization of the lattice i.e. an amorphous site may become crystalline after each time step.

The walk proceeds in this manner for the requisite number of steps. Due to the stochastic nature of the process, one has to average over a large number of such walks to get a meaningful value of $\langle r^2 \rangle$. In this work the walker does a random walk of (15000–75000) steps and distance (r) covered is averaged over (20000–100000) walks. This gives sufficiently good convergence (up to 3 significant figures) for the diffusion coefficient.

Our random walk algorithm allows the walker to move on an effectively infinite sample. This is possible because here we do not take a quenched system with sites assigned specifically to a definite phase. So the problem of finite size effects is avoided to some extent. But, of course there is a limitation to the size of the walk due to restricted computer time. For normal diffusion the relation between the diffusion coefficient and the conductivity is given by the Nernst–Einstein equation

$$\sigma = \frac{DNq^2}{kT}, \tag{3}$$

where N is the number density of the mobile ion, q is the charge of the mobile ion, k is the Boltzmann's constant and T is the temperature. The above equation is written as

$$\sigma = KXD, \tag{4}$$

3. Waiting times and jump distance in terms of the simulation parameters

A random walk is usually performed with the time step and lattice constant chosen to be unity for convenience. This will give D in terms of arbitrary units. To compare the value obtained with an experimental result, we must assign real values to τ and ξ. This section identifies these quantities in terms of experimentally measurable properties.

Our model lattice contains two types of sites, crystalline (c) and amorphous (a). The relative number of each depends on the salt fraction. Suppose τ is the time unit for the walk. Let the average waiting time for the amorphous and crystalline sites be $\langle \tau_a \rangle$ and $\langle \tau_c \rangle$ respectively. Let τ_j be the jump time between sites. Total time t for the walk is given by

$$t = N_c \langle \tau_c + \tau_j \rangle + N_a \langle \tau_a + \tau_j \rangle. \tag{5}$$

We assume here $\tau_j = \tau$ which is a constant. So eq. (5) becomes

$$t = N_c (t_c + 1)\tau + N_a (t_a + 1)\tau, \tag{6}$$

where N_c and N_a are respectively the total number of crystalline and amorphous sites visited during the walk. t_c and t_a are the waiting times measured in units of the jump time τ_j $(= \tau)$. Equation (6) can be written as

$$t = \tau (t_a + 1) \left[N_a + N_c \frac{(t_c + 1)}{(t_a + 1)} \right]. \tag{7}$$

Now $(t_c + 1)$ and $(t_a + 1)$ are nothing but inverse of the probability for a walker to jump from crystalline and amorphous sites respectively.

$$t_c + 1 = \frac{1}{p_c} : t_a + 1 = \frac{1}{p_a}, \tag{8}$$

where p_c and p_a are the jumping probabilities from crystalline and amorphous sites respectively. p_i may vary from 0 to 1, corresponding to the lowest and highest possible conductivities. For $p_i = 0$, t_i is ∞, the carrier getting permanently trapped and for $p_i = 1$, $t_i = 0$. We now define

$$\frac{t_a + 1}{t_c + 1} = \frac{p_c}{p_a} = \frac{1}{R}.$$

A time interval of N_t time steps corresponds to a real time interval of $N_t \tau$ seconds. To calculate τ, we use an estimate of $\tau (t_a + 1)$, obtained from NMR linewidth narrowing measurements [13–15]. This is a measure of the average time interval between successive jumps. Now we can use eq. (2) to calculate ξ, by comparing $(\langle r^2 \rangle / 4t)$ from our simulation, with a typical experimental value of D [16]. This gives $\xi = 6.14$ A which is

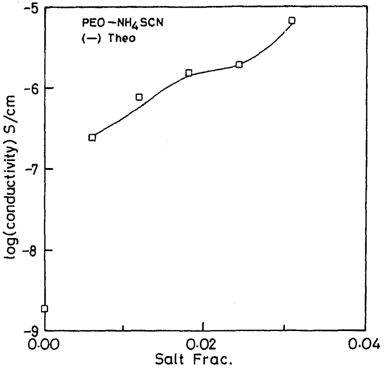

Figure 1. Plot of theoretical conductivity versus salt fraction for PEO–NH$_4$SCN. (□) show experimental results [4].

4. Results and discussion

Using the above algorithm we have calculated the diffusion coefficients as functions of salt fractions of two polymer electrolytes – PEO–NH$_4$SCN and PEO–NH$_4$I. The proportion of crystalline and amorphous sites for the simulation was obtained from experimental estimates of crystallinity from DTA measurements [3, 4]. The parameter R is as given in table 1. We find $R = 9.99$ gives satisfactory results in both cases showing that it is a property of the host polymer PEO. The conductivity is estimated using eq. (4). In eq. (4) X are taken from experiment [3, 4] and K is an arbitrary constant as given in table 1. The calculated values for conductivity fitted well with the experimental values (at room temperature) as shown in figures 1 and 2 [3, 4]. For a pure polymer i.e. zero salt fraction the conductivity according to our model is zero as it should ideally be. However experimental observations indicate [3, 4] that the pure polymer has non-zero conductivities for reasons mentioned in ref. [2, 17]. Our calculation could not be done for any other similar complex due to lack of experimental data of crystallinity (either from XRD or DTA).

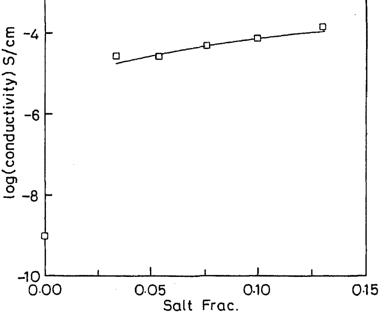

Figure 2. Plot of theoretical conductivity versus salt fraction for PEO–NH_4I. (□) show experimental results [3].

that the experimental crystallinity has been used as input for different salt fractions, in our simulation. It is necessary to predict the variation of crystallinity with salt fraction from a consistent theory or at least emperically to realise the full potential of our model.

The variation of crystallinity with X appears to be an interesting and complex problem in itself, since available results show peculiar irregularities and are often mutually contradicting [5]. We are at present working on this problem and expect to report our findings later. Some further shortcomings of our model are as follows. The effect of correlation of chain movements was not taken into account. Also from optical micrographs and x-ray difraction analysis it is usually found that the crystalline regions are in the form of spherullites [3]. Based on this, a better picture in the model would have been clustered groups of crystalline sites rather than a random distribution of single crystalline sites. However, in view of the dynamic disorder, our model appears realistic, because a single walker (i.e. a charge carrier) does not see the whole structure, but sees a small locality.

A useful extension of this model will be to incorporate variation of the renewal time, the time in which the structure rearranges itself. In its present form the renewal time is the shortest possible i.e. one time unit τ.

[2] C A Vincent, *Prog. Solid State Chem.* **17**, 145 (1987) and references therein

[3] K K Maurya, N Srivastava, S A Hashmi and S Chandra, *J. Mater. Sci.* **27**, 6357 (1992)

[4] N Srivastava, A Chandra and S Chandra, *Phys. Rev.* **B52**, 225 (1995)

[5] D Prusnikowska, W Wieczorec, H Wycislik, M Siekerski and J Przyluski, *Solid State Io* **72**, 152 (1994)

[6] J P Bouchaud and A Georges, *Phys. Rep.* **195**, 127 (1990)

[7] S Havlin and D Ben-Avraham, *Adv. Phys.* **36**, 695 (1987)

[8] J W Haus and K W Kehr, *Phys. Rep.* **150**, 263 (1987)

[9] J F McCarthy, *J Phys.* **A26**, 315 (1986)

[10] S D Druger, A Nitzan and M A Ratner, *J. Chem. Phys.* **79**, 3133 (1983)

[11] S D Druger, M A Ratner and A Nitzan, *Phys. Rev.* **B31**, 3939 (1985)

[12] Aninda Jiban Bhattacharyya and S Tarafdar, to be published

[13] J B Boyce and B A Huberman, *Phys. Rep.* **51**, 189 (1979)

[14] S H Chung, K R Jeffrey and J R Stevens, *J. Chem. Phys.* **93**, 1803 (1991)

[15] C Wang, Q Liu, Q Cao, Q Meng and L Yang, *Solid State Ionics* **53–56**, 1106 (1992)

[16] W Gorecki, R Andreani, C Berthier, M Armand, M Mali, J Roos and D Brinkmann, *S State Ionics* **18-19**, 295 (1986)

[17] S Chandra, S A Hashmi and G Prasad, *Solid State Ionics* **40–41**, 651 (1990)

Spectroscopic study of β-Ni(OH)$_2$ under pressure

CHITRA MURLI, V SUGANDHI*, NANDINI GARG,
SURINDER M SHARMA and S K SIKKA
High Pressure Physics Division; *Spectroscopy Division, Bhabha Atomic Research Centre,
Mumbai 400 085, India
Email: hppd@magnum.barct1.ernet.in

MS received 4 August 1997

Abstract. Infrared absorption and Raman study of β-Ni(OH)$_2$ has been carried out up to 25 GPa and 33 GPa, respectively. The frequency of A_{2u} internal antisymmetric stretching O–H mode decreases linearly with pressure at a rate of $-0.7\,\mathrm{cm}^{-1}$/GPa. The FWHM of this mode increases continuously with pressure and reaches a value of $\sim 120\,\mathrm{cm}^{-1}$ around 25 GPa. There was no discernible change observed in the frequency and width of the symmetric stretching A_{1g} O–H Raman mode up to 33 GPa. The constancy of the Raman mode is taken as a signature of the repulsion produced by H–H contacts in this material under pressure. Lack of any discontinuity in these modes suggests that there is no phase transition in this material in the measured pressure range.

Keywords. β-Ni(OH)$_2$; phase transition; infrared absorption; Raman study; high pressure.

PACS Nos 78.30; 62.50

1. Introduction

High pressure study of mineral dihydroxides M(OH)$_2$ (where M = Mg, Ca, Co, Ni, etc.,) is of importance for understanding the nature of hydrous minerals under compression in the earth's interior. These hydroxides crystallize in trigonal CdI$_2$ structure with space group $P\bar{3}m1$ [1]. β-Ni(OH)$_2$ belongs to this family of compounds. It is widely used in nickel batteries because of the unusually high level of activity of hydrogen atoms in this material. It is therefore of interest to understand the high pressure behaviour of hydrogen sublattice in this material. As hydrogen atoms are insensitive to x-ray diffraction techniques, neutron diffraction study of hydroxide compounds is an effective tool for understanding the behaviour of hydrogen sublattice of these compounds under different thermodynamic conditions. However, a simpler technique is the vibrational spectroscopic technique. In this method the reduction in the frequency of O–H mode with pressure is correlated with the enhancement of hydrogen bonding under pressure. This technique also throws light on the pressure induced phase transitions. High pressure studies reported in recent years have revealed pressure induced hydrogen disordering of Ca(OH)$_2$, Mg(OH)$_2$ and Co(OH)$_2$. In polycrystalline samples of Ca(OH)$_2$ pressure induced

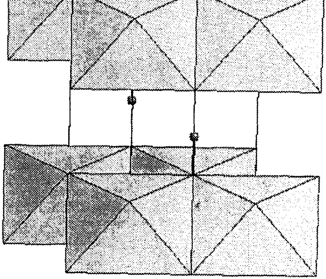

Figure 1. The crystal structure of β-Ni(OH)$_2$. Hydrogen atoms are shown along with the Ni–O octahedra with the corner positions occupied by oxygen atoms and nickel atoms in the centre. Nickel and oxygen atoms are not shown for the purpose of clarity.

beyond 20 GPa [3]. Mg(OH)$_2$ is reported to be stable up to 80 GPa with no signature of amorphization [4]. However, disordering of hydrogen sites involving shift of H positions away from the three fold axis in the $P\bar{3}m1$ structure around 1 GPa has been detected by spectroscopic studies of this compound [5]. This is confirmed by a neutron diffraction study which gives evidence of a hydrogen disordering around 5–10 GPa [6]. In Co(OH)$_2$ infrared and Raman spectroscopy under pressure document that the hydrogen sublattice loses long range order between 7 to 11 GPa [7]. However, x-ray diffraction shows that Co–O sublattice is ordered up to 30 GPa. In the $P\bar{3}m1$ structure, there are two allowed internal hydroxyl stretching modes, the Raman active A_{1g} symmetric stretching mode where hydroxyl ions vibrate in phase and the A_{2u} antisymmetric stretching infrared mode where the hydroxyl ions vibrate out of phase. The A_{2u} antisymmetric stretching internal OH mode in β-Ni(OH)$_2$ is observed at 3645 cm^{-1} which is higher than the value of 3570 ± 10 cm^{-1} for an unperturbed OH$^-$ ion [8]. The larger value is indicative of the repulsive effect of the lattice due to short H–H contact of 1.92 Å [12] at 0.1 MPa between layers of Ni–O octahedra (figure 1) and of weak hydrogen bonding in the system. To understand the high pressure behaviour of this compound we have carried out infrared absorption and Raman spectroscopic studies.

2. Experimental

IR absorption study was carried out using BOMEM DA3.003 FTIR spectrometer with a globar source and InSb detector. The resolution setting was 2 cm^{-1} in the spectral region 3400–3800 cm^{-1} of our study. The IR absorption data were analysed using a

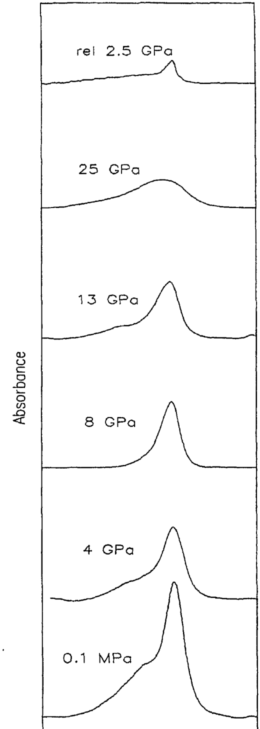

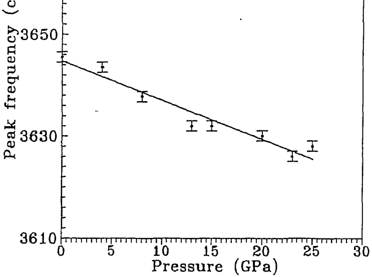

Figure 3. The change in frequency of A_{2u} mode of β- $Ni(OH)_2$ with pres

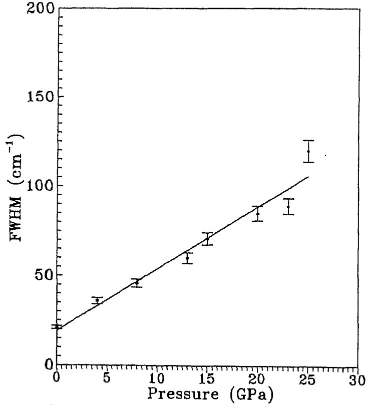

Figure 4. Variation of FWHM of A_{2u} mode of β-$Ni(OH)_2$ with pressure.

spectracalc software package. Raman study was carried out using a single stage

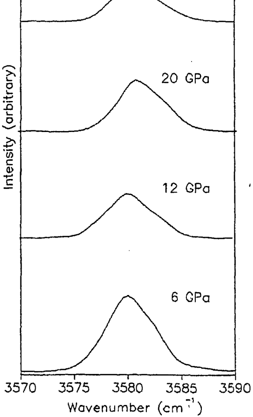

Figure 5. A_{1g} symmetric stretching internal Raman hydroxyl mode of β-$Ni(OH)_2$ at different pressures.

tube and a computer controlled data acquisition system. The A_{1g} Raman mode under ambient conditions was found to be $3580\,cm^{-1}$ which is consistent with the value reported earlier [11].

3. Results and discussion

The IR absorption spectrum of β-$Ni(OH)_2$ could be followed up in a diamond anvil cell up to 25 GPa in the region 3400 to $3800\,cm^{-1}$. The IR absorption spectrum under ambient conditions was recorded and the frequency of the A_{2u} mode was determined to be $3645\,cm^{-1}$ which is in good agreement with the values reported earlier [12]. Figure 2 shows this mode at different pressures. The asymmetry on the lower frequency side is due to particle size effect [12]. The frequency of this mode decreases linearly with pressure (figure 3) at a rate of $-0.7\,cm^{-1}/GPa$. This is unlike $Co(OH)_2$ which shows a discontinuity around 11 GPa. The FWHM of this mode increases continuously with pressure and reaches a value of $120\,cm^{-1}$ around 25 GPa (figure 4). This behaviour is similar to that of

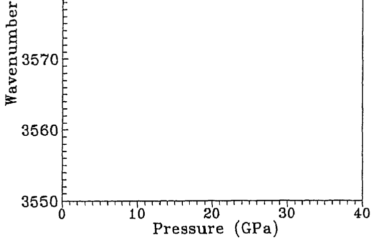

Figure 6. Frequency of A_{1g} Raman mode versus pressure for β-Ni(OH)$_2$.

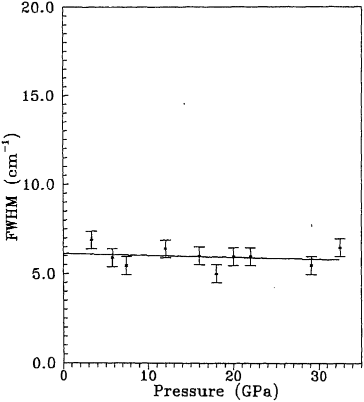

Figure 7. FWHM of A_{1g} mode of β-Ni(OH)$_2$ versus pressure.

The A_{1g} Raman mode observed at 3580 cm^{-1} under ambient conditions was recorde up to a pressure of 33 GPa (figure 5). The frequency as well as FWHM of this mod was found to remain nearly constant in this pressure range (figures 6 and 7) in contrast t

Material	ν_{OH}(cm^{-1})		$d\nu_{OH}/dp$ (cm^{-1}/GPa)	
	IR	Raman	IR	Raman
$Mg(OH)_2$	3688	3652	−0.6	−7.68
$Ca(OH)_2$	3633	3620	−3.5	−3.68
$Co(OH)_2$	3631	3570	∼ −2.3	∼ −4.00
β-$Ni(OH)_2$	3645	3580	−0.7	0.00

the reported disappearance of this mode below 10 GPa in $Co(OH)_2$ and $Ca(OH)_2$. Thus the persistence of this mode suggests lack of any signature of a structural change. The negligible change in the frequency of this mode is in contrast to the observations for other hydroxides (table 1). This can be interpreted as a signature of repulsion produced by decreasing H–H contacts under pressure [13, 14]. This observation is also supported by x-ray diffraction studies carried out in our laboratory [9]. The c/a value was found to be almost pressure independent. The material was found to be very less compressible up to a pressure of 33 GPa. The bulk modulii K_0, K_{0c} and K_{0a} of the sample were determined to be ∼221 GPa, 379 GPa and 1391 GPa respectively using Birch–Murnaghan equation of state [9]. These values are the largest compared to the other reported dihydroxide compounds [9] and indicate that this compound is very stiff in this family of compounds.

4. Conclusion

Lack of any discontinuity observed in the frequency and FWHM of IR and Raman hydroxyl modes in β-$Ni(OH)_2$ suggests that there is no phase transition in this compound up to 33 GPa. The increase in the FWHM of the A_{2u} IR mode is indicative of a slow hydrogen disordering of this compound with pressure. The negligible change in the values of A_{1g} Raman mode is a signature of the repulsion produced by decreasing H–H contacts in this compound under pressure.

References

[1] H E Petch and H D Megaw, *J. Opt. Soc. Am.* **44**, 733 (1954)
[2] C Meade and R Jeanloz, *Geophys. Res. Lett.* **17**, 1157 (1990)
[3] S K Ekbundit, K Leinenweber, J L Yarger, J S Robinson, M Verhelst-Voorhees and G H Wolf, *J. Solid State Chem.* **126**, 300 (1996)
[4] Y Fei and H K Mao, *J. Geophy. Res.* **98 B7**, 11875 (1993)
[5] T S Duffy, C Meade, Y Fei, H K Mao and R J Hemley, *Am. Mineral* **80**, 222 (1995)

and x-ray diffraction in bismuth thin film

K JAYACHANDRAN and C S MENON
School of Pure and Applied Physics, Mahatma Gandhi University, Kottayam 686 560, India
Email: mgu@md2.vsnl.net.in

MS received 10 April 1997; revised 29 January 1998

Abstract. Spectroscopically pure bismuth is evaporated onto glass substrates at different substrate temperature using a Hind Hivac coating plant. The electrical conductivity of bismuth thin films, prepared at different substrate temperatures is measured and thermal activation energy is evaluated. From the recorded optical absorption spectrum in the ultraviolet and visible regions optical band gap E_g is determined. X-ray diffractograms are recorded and lattice parameters are determined.

Keywords. Thin film; electrical conductivity; optical absorption; x-ray diffraction.

PACS Nos 68.60; 73.60; 78.65

1. Introduction

Bismuth is a semimetal. Semimetals are a class of solids which are used to probe the Fermi surface and the band structure of the crystalline solids [1]. The narrow band gap of bismuth and its alloys find applications in Hall effect devices, hyper frequency power sensors, thermopiles and microwave detectors [2]. The electrical, optical and structural studies of bismuth thin films have been reported by many authors [3, 4]. But the studies made earlier on bismuth thin films have large inconsistencies. In this paper a systematic study is reported on the electrical, optical and structural properties of bismuth thin film.

2. Experimental

Thin films of bismuth are prepared by vacuum evaporation of 99.999% pure bismuth (obtained from SISCO) by resistive heating method. The evaporation is carried out from a molybdenum boat at a pressure of 10^{-5} torr. Substrate temperature is varied by a controlled variac arrangement and temperature is monitored by a copper-constantan thermocouple. The thickness of the film is determined by Tolansky's interference technique [5]. Electrical connections are given using silver paste and conductivity measurements have been done using a four probe set-up (DFP-02). The conductivity is measurements are carried out for the films prepared at substrate temperatures 75, 100, 200 and 250°C. Figure 2 shows the plot of electrical conductivity vs temperature for Bi film prepared at substrate temperature 100°C. It is observed that the conductivity increases first, then decreases followed by a sharp increase, in the temperature range 30 to 250°C. The semiconducting region is absent in the cooling cycle. The same behaviour is observed for the films prepared at substrate temperatures of 75, 150, 200 and 250°C. Thin film consists of individual islands which have many of the characteristics of the liquid droplets. As the substrate temperature increases, the contact angle between droplet and substrate decreases and the droplet grows in size. Thus a given amount of material deposited on a substrate at low temperature may be enough to form a continuous film, whereas the same amount of material deposited on a hotter substrate will result in an

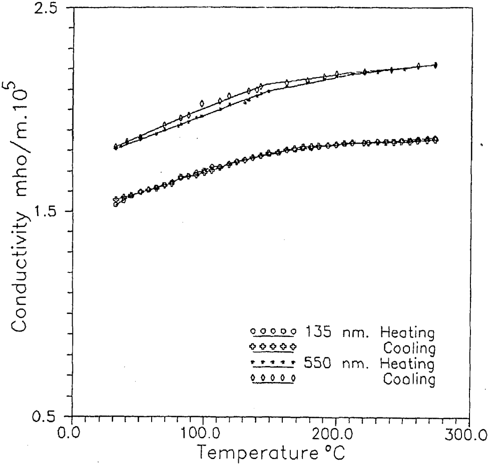

Figure 1. Plot of conductivity (σ) versus temperature (T) for bismuth film coated at room temperature.

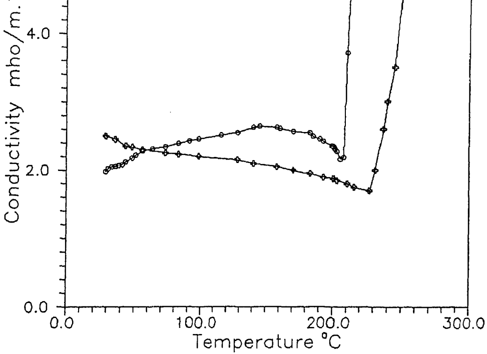

Figure 2. Plot of σ versus T for bismuth film coated at substrate temperature of 100°

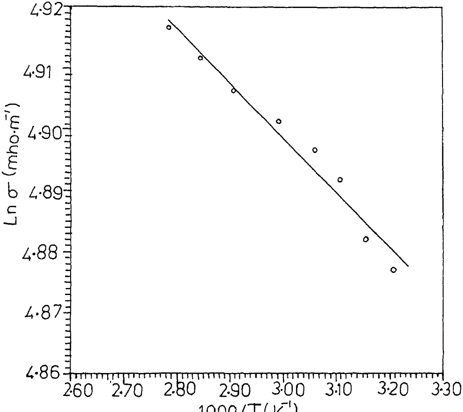

100	7.76
150	6.81
200	6.03
250	5.17

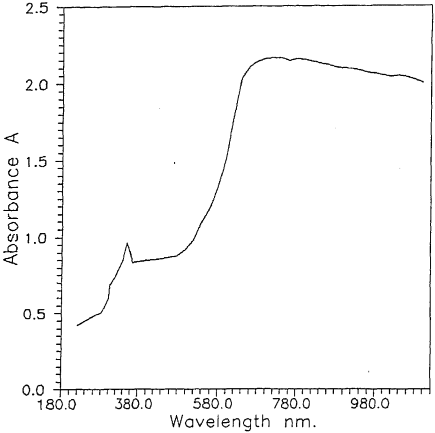

Figure 4. The optical absorption spectrum of Bi film.

island structure. The jumps in conductivity are due to coalesence of islands. Similar results have been observed by Das and Jagadeesh [6] for Bi–Sb alloy films.

Thermal activation energy is related to the electrical conductivity according to Arrhenius relation,

$$\sigma = \sigma_0 \exp[-\Delta E/kT],$$

where σ_0 is a constant, ΔE is the thermal activation energy and k the Boltzmann constant. Graph is plotted with $\ln \sigma$ along y axis and $1000/T$ along x axis as shown in figure 3. From the slope of the graph activation energy is calculated. The effect of substrate temperature on thermal activation energy is shown in table 1.

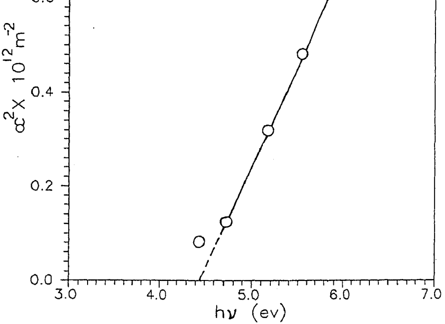

Figure 5. Plot of α^2 versus $h\nu$ for Bi film.

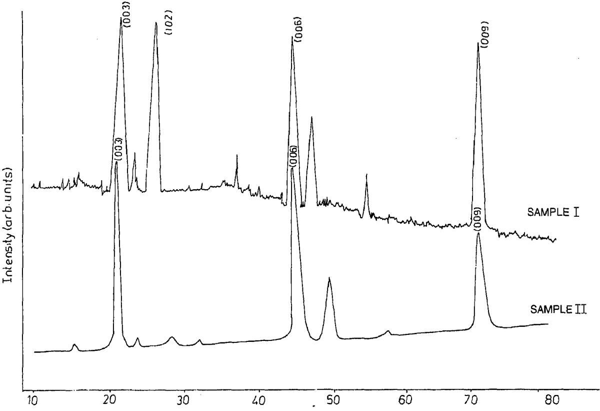

200	60.1
250	47.5

the optical band gap E_g by the relation

$$\alpha = \alpha_0(h\nu - E_g)^n,$$

where $n = 1/2$ for direct allowed transition and E_g is the optical band gap. Graph of α^2 versus $h\nu$ is plotted as shown in figure 5 and is extrapolated to zero absorption to obtain the optical band gap. The optical band gap E_g is obtained as 4.45 eV for bismuth thin film. Similar results have been obtained by Al Houty *et al* [2] for the energy band gap of bismuth thin film.

X-ray diffractogram is recorded for the bismuth thin film of 200 nm thickness and is shown in figure 6. From the XRD pattern it is evident that bismuth has high degree of preferential orientation with the basal plane parallel to the film plane, indicating strong reflection from (003), (006) and (009) planes [3]. The lattice spacing d is calculated and compared using the standard ASTM data. Lattice constants are obtained for hexagonal bismuth as $a = 4.54$ Å and $c = 11.85$ Å. Grain size (L) of the film is calculated using Scherrer formula [7].

$$L = K\lambda/\eta_{1/2}\cos\theta,$$

where K is a constant equal to 0.9, $\eta_{1/2}$ is the full width at half maximum intensity and θ corresponds to the Bragg angle. The grain size is calculated for the films prepared at different substrate temperatures and is given in table 2.

References

[1] J P Issi, *Aust. J. Phys.* **32**, 585 (1979)

[2] L Al Houty, M E Kaseem and H I Abdel Kader, *J. Mater Sci.* **6**, 17 (1995)

[3] V Damodara Das and N Soundararajan, *Phys. Rev.* **B35**, 5990 (1987)

[4] R Atkinson and P H Lossberger, *Thin Solid Films* **17**, 107 (1971)

[5] S Tolansky, *Multiple beam of interference microscope of metals* (Academic Press, London, 1970)

[6] V Damodara Das and M S Jagadeesh, *Mater Res. Bull.* **16**, 1547 (1981)

[7] B D Cullity, *Elements of x-ray diffraction* (Addisson–Wesley Publ. Company Inc., 1978)

Hyperfine interaction study of electric field gradient in hafnium phosphide using ^{181}Ta probe

VIVEK MANDOT, S N A JAAFFREY*, S S SHARMA and J VARMA
Department of Physics, College of Science M L Sukhadia University, Udaipur 313 001, India
* Address for correspondence: 2A, Sector 14, Hiran Magari (Goverdhan Vilas), Udaipur 313 001, India
Email: phy@mlsu.ac.in

MS received 1 May 1997; revised 13 January 1998

Abstract. The hyperfine interaction of ^{181}Ta in HfP has been investigated by time differential perturbed angular correlation method which yielded interaction frequency $\nu_Q = 630.20(15)$ MHz. The observed electric field gradient is calculated to be $1.66(25) \times 10^{20}\,\mathrm{V/m^2}$.

Keywords. Electric field gradient; asymmetry parameter; hafnium; phosphorus; hyperfine interaction; interaction frequency; quadrupole interaction; TDPAC.

PACS No.

1. Introduction

In recent years there has been increased interest in the hyperfine interaction studies of electric field gradient in compound systems [1–3]. A number of studies have been made in phosphides to understand the environment of phosphorus in compound such as TiP, ZrP, TaP, NbP, etc. [4]. The environment of the phosphorus in these compounds is more likely the trigonal prism. The tendency of phosphorus towards self-linkage is found only in these phosphorus rich phases in which pairs of atoms or chains usually occur [5, 6]. Authoritative reviews of metal phosphides are available, which cover the studies of the phosphides of group fourth, fifth and sixth and deal with the binary phosphides of all transition metals [7–9].

Moreover titanium and zirconium phosphides, to which the sodium chloride structures are ascribed, are reported to be probably phosphorus deficient [10]. The occurrence of this structure in transition metal monophosphides and the existence of an essentially undistorted octahedral environment for phosphorus in TiP seems to provide a transition from the lanthanide phosphide (all of which have the NaCl type structure) to the transition metal phosphides. Further it suggests that at least some of the phosphorus in group four B compounds could be in the ionic $P^{(-3)}$ form. Since Hf belongs to group four B and is very similar to Zr and Ti, the hyperfine interaction study was planned to find be 10.8 ns.

2. Experimental

Hafnium monophosphide systems were prepared by heating together hafnium powder and red phosphorus in sealed quartz tube under vacuum at 900°C for 12 h and quenched in water at 20°C. The TDPAC spectra of the samples were acquired at room temperature using a four counter set up. All spectra turned out to be same in identical conditions. The usual asymmetry ratio of the coincidence spectra at the angles 90° and 180° has been formed in each case. The time resolution of system was found to be 2.3 ns (FWHM). After subtracting the chance coincidence, the ratio $A_{22}G_{22}(t)$ was calculated as defined below

$$A_{22}G_{22}(t) = \frac{2^*[W(180,t) - W(90,t)]}{[W(180,t) + 2^*W(90,t)]},$$

where $W(180,t)$ and $W(90,t)$ are coincidence counts at angles 180° and 90° respectively and t is the time delay between the two gamma photons. The data in figure 1 were

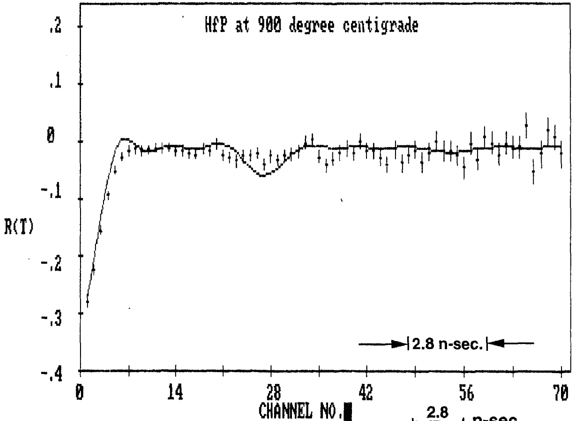

The figure shows one of the spectra of the sample treated at temperature 900°C which developed into well-defined frequency. Computer analysis yielded frequency 630.20 (15) MHz and very small spread in interaction frequency of 1.5%, which clearly rules out the possibility of phosphorus deficient structure of HfP. From the interaction frequency, EFG in HfP is estimated using Sterheimer antishielding factor $(1 - \gamma_\infty) = 62$ [11, 12] and quadrupole moment 2.5 (0.15) barn [13] to be $1.66(0.25) \times 10^{20}$ volt/m^2. This EFG was compared with theoretically obtained EFG 1.72×10^{20} volt/m^2 for well known hexagonal closed pack HfP system using lattice parameters $a = 3.65$ Å, $c/a = 3.39$ Å and phosphorus in $P^{(-5)}$ form [14–16]. The consistency between the observed and computed EFG's allowed us to draw conclusion about the phosphorus ionic form in HfP system to be more likely the $P^{(-5)}$ rather than the $P^{(-3)}$ form.

Moreover the high value of $A_{22}(t) = -0.25$ at $t = 0$ and asymmetry parameter $\eta = 0$ also support the strong quadrupole interaction of ^{181}Ta with EFG in HfP and non-existence of undistorted environment. The inherent value of $\lambda = -0.015$ could probably be attributed to the relaxation of charges in the system during beta decay of ^{181}Hf nuclei. It could be explained by the time dependent electric quadrupole interaction during charge neutralization process of ions ($\tau = 5 \times 10^{(-8)}$ s) [17].

Acknowledgement

The authors are thankful to Drs Gufran Beig and K Venugopalan for valuable discussion and computer analysis of data.

References

[1] A Lerf and T Butz, *Hyperfine Interaction* **36**, 275 (1987)
[2] J W Ball and M Kaplan, *J. Chem. Phys.* **69**, 117 (1978)
[3] A Baudry, P Boyer and J P Boilot, *Solid State Commun.* **56**, 91 (1985)
[4] *M T P International Review of Science* (Inorganic Chemistry Series One) *Transition Metals – Part 1* edited by W A Sharp (University Park Press, Baltimore, 1972) vol. 5, pp. 152–162
[5] P O Snell, *Actachem. Scand.* **21**, 1773 (1967)
[6] N Schonberg, *Actachem. Scand.* **8**, 226 (1954)
[7] T Lundström, *Ark. Kemi.* **31**, 227 (1969)
[8] S Rundquist, *Ark. Kemi.* **20**, 67 (1963)
[9] I Engström, *Thesis* (University of Uppsala, 1970)
[10] R Steffen and H Frauenfelder, *Alpha, beta and gamma ray spectroscopy* edited by Kai Siegbahn (North-Holland Publishing Company, Amsterdam, 1965), vol. 2, p. 997
[11] K Sen and P T Narasimhan, *Phys. Rev.* **B15**, 96 (1977)
[12] F D Feiok and W R Johnson, *Phys. Rev.* **187**, 39 (1969)
[13] G Netz and E Bodenstedt, *Nucl. Phys.* **A208**, 503 (1973)

1967) pp. 1076

Mean lifetime measurements of F II and F III levels using beam-foil technique

B N RAJA SEKHAR, S PADMANABHAN, APARNA SHASTRI, P MEENAKSHI
RAJA RAO†, M B KURUP* and K G PRASAD*
Spectroscopy Division, Bhabha Atomic Research Centre, Trombay, Mumbai 400 085, India
*Tata Institute of Fundamental Research, Colaba, Mumbai 400 005, India
†Address for correspondence
Email: spectr@magnum.barct1.ernet.in

MS received 14 October 1997

Abstract. Beam-foil spectrum of fluorine was recorded in the wavelength region of 2000–4500 Å using F^+ ion beams of energies ranging from 216 to 296 KeV. Some of the spectral lines of fluorine observed during the present investigation are hitherto unknown. Mean lifetimes of a few of the excited levels of F II and F III are reported for the first time.

Keywords. Beam-foil spectroscopy; fluorine; lifetimes.

PACS Nos 32.70; 34.50

1. Introduction

The earliest published results on the lifetimes of the energy levels of fluorine were by Kaselevskii and Trukhan [1]. They reported *f*-values for lines from F II–F V in the wavelength region 2450–3450 Å. The results were based on experiments carried out in emission using a pulsed capillary discharge source and photographic detection. Due to the uncertainty in measuring line intensities, particle densities and temperature, their estimated *f*-values were in error by 35–40%. Kurucz and Peytremann [2] have evaluated semiempirical *gf*-values for a few fluorine transitions. Smith and Wiese [3] have studied the transitions that are isoelectronic with fluorine but they could not establish any trend for *f*-values. Pinnington *et al* [4, 5] have carried out beam-foil measurements of lifetimes of several transitions belonging to F II–F IV in the wavelength region of 2100–4500 Å. The authors evaluated the lifetimes by correcting the effects of cascade repopulation using ANDC method and theoretically calculated the corresponding lifetimes under the Coulomb approximation. However the theoretical and the accelerator at TIFR. The experimental arrangement for recording the beam-foil spectrum has been described in detail elsewhere [6]. SF_6 gas was used in the ion source for extracting mass analysed F^+ ion beams. The F^+ beam was collimated and passed through carbon foils of thickness 6 to 8 $\mu g/cm^2$. The emitted spectra were recorded on a 0.45 M monochromator in Czerny–Turner mount and a Peltier cooled photomultiplier was used as a detector. The photomultiplier was used in the single photon counting mode and spectra were recorded using a PC based multiscaling system. For lifetime studies the beam-foil light was focussed onto the entrance slit of the monochromator by means of a quartz lens in 1 : 1 magnification. Taking into account the energy loss suffered by the ions while passing in the foil and using the computer code TRIM [7], the post foil velocities of the ions were calculated. These calculated velocities were used to extract level lifetimes. During all these lifetime measurements a constant beam current $\sim$40 nA was maintained. The photon counts at each measured distance downstream the foil were normalized to the incident ion beam intensity measured by a current integrator and a deep Faraday cup located behind the foil. The target chamber containing the carbon foils was evacuated using a cryo pump up to a pressure of 10^{-6} torr. The holder on which the foil was mounted has a provision for linear movement along the beam axis to facilitate mean lifetime measurement and also facility to change the foil in vacuum. The experimental data was analysed using a multi exponential fitting program and the lifetimes were derived from the fitted data after background correction.

3. Results and discussion

3.1 *Wavelength spectrum*

Beam-foil spectrum of fluorine was recorded at three energies i.e. 216, 256 and 296 KeV in the wavelength range of 2000–4500 Å. Typical spectrum in the region of 2950–3250 Å is shown in figure 1. The spectrum consisted mainly of lines due to F II and F III. Most of the lines observed for the first time in the present studies fall in the region of 4900 to 5000 Å and are shown in figure 2. A core-excited transition at 2656.2 Å belonging to F III was also observed. The spectral features were carefully examined for possible blending and spectral lines which were free from blending were chosen for lifetime determinations. The observed wavelengths were compared and identified with the data reported by Palenius for F II and F III [8, 9]. The notations and terminology followed are the ones used in the references [8] and [9].

3.2 *Mean lifetimes*

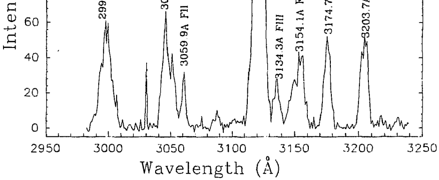

Figure 1. Beam-foil spectrum of fluorine in 2950–3250 Å region.

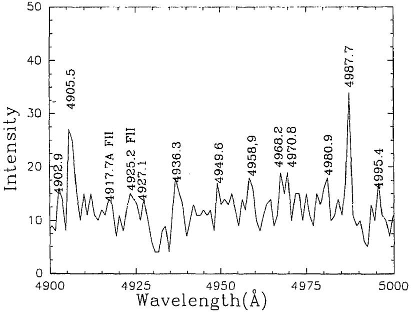

Figure 2. New lines observed in fluorine in 4900–5000 Å region.

out spectral line blending and cascading problems and serves as a cross check. In the present investigations, different measurements agreed within 10%. The values included in table 1 refer to an average value of all the measurements considered.

3.2.1 *FII*: Mean lifetimes of components of six energy levels of singly ionized fluorine were evaluated and they are listed in table 1. Lifetimes for two lines 3972.1 and 4024.7 Å involving the $2s^22p^3(^2P)3\bar{\bar{p}}\ ^3D$ and $2s^22p^3(^4S)3p\ ^3P$ lines respectively were reported by Pinnington *et al* [4] and our values agree well with their values. Figure 3 shows the decay curve for 4024.7 Å. The mean lifetimes measured for the lines at 3202.7, 3473.3 and

	3971.6	$2s^2 2p^3(^2P)3\bar{\bar{p}}\ ^3D_{1,2}$	6.92 ± 0.1	$8.50^{+\#}, 7.80^{+@}$
	3972.0	$2s^2 2p^3(^2P)3\bar{\bar{p}}\ ^3D_{1,2}$		$6.90 \pm 0.6^{\#}$
	3972.4	$2s^2 2p^3(^2P)3\bar{\bar{p}}\ ^3D_{1,2}$		
	3972.7	$2s^2 2p^3(^2P)3\bar{\bar{p}}\ ^3D_{1,2}$		
	4024.7	$2s^2 2p^3(^4S)3p\ ^3P_{0,1,2}$	7.35 ± 0.2	$8.20 \pm 0.7^{\#}$
	4025.0	$2s^2 2p^3(^4S)3p\ ^3P_{0,1,2}$		$8.30^{+\$}, 7.80^{+@}$
	4025.5	$2s^2 2p^3(^4S)3p\ ^3P_{0,1,2}$		
	4112.7	$2s^2 2p^3(^2D)3\bar{p}\ ^3D_{3,2}$	8.31 ± 0.2	
	4112.9	$2s^2 2p^3(^2D)3\bar{p}\ ^3D_{3,2}$		
	4299.2	$2s^2 2p^3(^2D)3\bar{p}\ ^1F_3$	11.5 ± 0.4	$10.41 \pm 0.7^{\#\#}$ $11.0 \pm 1.0^{\$\$}$ $10.5^{+\$\$}, 9.7^{+@}$
F III	2592.8	$2s^2 2p^2(^3P)3d\ ^4F_{3/2,5/2}$	3.82 ± 0.1	
	2593.2	$2s^2 2p^2(^3P)3d\ ^4F_{3/2,5/2}$		
	2629.7	$2s^2 2p^2(^1D)3\bar{d}\ ^2G_{9/2}$	4.10 ± 0.1	$2.50^{+\$\$}$, 2.20^{+*}, $3.70 \pm 0.4^{\$\$}$ 4.10^{+**}
	2656.0	$2s2p^3(^5S)3d'\ ^6D_{9/2,7/2,5/2}$	3.37 ± 0.1	$3.3 \pm 0.3^{\$\$}$
	2656.3	$2s2p^3(^5S)3d'\ ^6D_{9/2,7/2,5/2}$		$2.7^{+\$\$}$
	2656.4	$2s2p^3(^5S)3d'\ ^6D_{9/2,7/2,5/2}$		
	2877.3	$2s^2 2p^2(^3P)4p\ ^2D_{3/2}$	5.95 ± 0.1	
	2916.3	$2s^2 2p^2(^3P)3p\ ^4P_{5/2}$	3.86 ± 0.2	
	3115.7	$2s^2 2p^2(^3P)3p\ ^4D_{5/2}$	7.27 ± 0.2	
	3154.4	$2s^2 2p^2(^1D)3\bar{d}\ ^2D_{5/2}$	4.48 ± 0.1	

** [1], @ [2], * [3], $$ [4], # [5], ## [10], $ [11], † Theory.

4112.8 Å involving $2s^2 2p^3(^2D)3\bar{p}\ ^1D_2$, $2s^2 2p^3(^2D)3\bar{d}\ ^3F$ and $2s^2 2p^3(^2D)3\bar{p}\ ^3D$ are being reported for the first time.

3.2.2 *FIII*: Mean lifetime measurements for 7 levels of doubly ionized fluorine are experimentally determined and they are included in table 1. Two of the levels investigated by us viz. levels involved in the transitions at 2629.7 and 2656.2 Å were reported earlier by Pinnington *et al* [5]. The measured values during the present studies are in close agreement with the reported results. The decay curves for the energy levels involved in

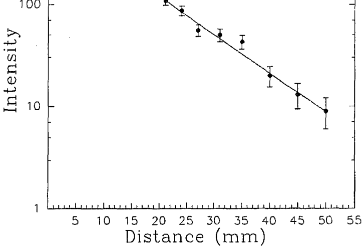

Figure 3. Decay curve of 4024.7 Å (F II) line.

lines at 2877.3 and 2916.3 Å, studied for the first time during present investigations exhibit cascading. The secondary lifetimes corresponding to cascading transitions are of the order of 15 ns. The 2877.3 Å line with the upper state $2s^22p^2(^3P)4p\ ^2D_{3/2}$ has its main cascading contribution from $2s^22p^2(^3P)5s\ ^2P_{1/2}$. Even though the transition at 4221.1 Å involving $4p\ ^2D_{3/2}$-$5s\ ^2P_{1/2}$ was observed in our spectrum, it was blended with an F II line at 4221.5 Å ($3\bar{d}\ ^3F_2 - 4\bar{f}(5/2)[5/2]_3$) thus making the lifetime determination of the level $2s^22p^2(^3P)5s\ ^2S_{1/2}$ impossible. For the 2916.3 Å line the upper state is $2s^22p^2(^3P)3p\ ^4P_{5/2}$, and the cascading is from the $2s^22p^2(^3P)3d\ ^4D$, $2s^22p^2(^3P)3d\ ^4P$ and $2s^22p^2(^3P)3\bar{d}\ ^2F$ levels. Lifetime determination of the cascading levels was not possible in our present experiment as most of these transitions fall in the vacuum ultraviolet region. The mean lifetimes of transitions involving the $2s^22p^2(^3P)3p^4D$, $2s^22p^2(^3P)3d\ ^4F$ and $2s^22p^2(^1D)3\bar{d}\ ^2D$ levels are reported for the first time.

3.3 *Excitation function studies*

Beam-foil excitation copiously populates highly excited levels of several charge states. The source is of low intensity thereby necessitating the use of medium resolution monochromators. Therefore, line blending problems are very severe in beam-foil spectra. Blending of lines within the same as well as different charge states is very common. In order to sort out such problems during the present studies excitation function studies were carried out. For the excitation function studies the signal was collected very close to the foil so as to minimize the influence due to cascade repopulations and the intensity variation as a function of excitation energy was studied. The details of the procedure followed are discussed elsewhere [12]. The line at 3042.8 Å was reported by Pinnington

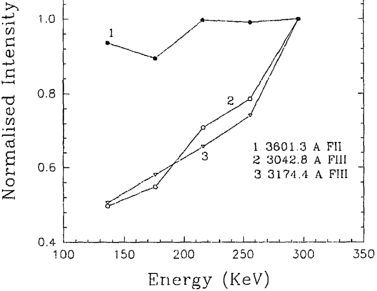

Figure 4. Comparative study of the relative level population of 3042.8 Å with 3601.3 Å (F II) and 3174.4 Å (F III) lines.

FIV based on the spectra taken at 2 and 3 MeV. Excitation function studies were rried out comparing the relative level populations for F II and F III with that of the ansition at this wavelength (3042.8 Å) with all the relative level populations normalized unity at 296 KeV. In the wavelength spectra recorded by us no lines belonging to F IV ere observed. From the comparison of excitation functions as shown in figure 4, it can concluded that the transition at 3042.8 Å belongs to F III. Thus it appears that at lower citation energies viz. in the KeV range, F III transition is observed whereas at higher ergies in the MeV region F IV transition was predominant.

Conclusion

he beam-foil spectra of F II and F III in the region of 2000–4500 Å were recorded. The udies lead to identification of new lines belonging to fluorine. The mean lifetimes of ree terms of F II and five terms of F III are reported for the first time.

cknowledgements

he authors thank Dr. A P Roy, Spectroscopy Division for his keen interest and ncouragement during the course of this work. The authors are grateful to C A Desai for s valuable assistance in operating the 400 KeV accelerator.

[6] T Nandi, V Nanal, W A Fernandes, C A Desai, M B Kurup, K G Prasad, P M R Rao and S Padmanabhan, *Pramana – J. Phys.* **44**, 67 (1975)

[7] J F Ziegler and J P Bievack, The stopping and range of ions in solids (Pergamon Press, New York, 1990)

[8] H P Palenius, *Arkiv. Fysic. Band* **39**, 3 (1968)

[9] H P Palenius, *Phys. Scr.* **1**, 113 (1970)

[10] S A Chin-Bing and C E Head, *Phys. Rev.* **A10**, 209 (1974)

[11] W L Wiese, M W Smith and B M Glennon, *Natl. Stand. Ref. Data. Ser. Natl. Bur. Stand. 4* (US Government Printing Office, Washington, DC, 1975) vol. I

[12] B N Raja Sekhar, S Padmanabhan, Aparna Shastri, P Meenakshi Raja Rao, M Jagadeesh, M B Kurup and K G Prasad, *Indian J. Phys.* **71B**, 651 (1997)

[13] S Bashkin, *J. Phys.* **C1**, 125 (1979)

Third harmonic generation in layered media in presence of optical bistability of the fundamental

JOLLY JOSE and S DUTTA GUPTA
School of Physics, University of Hyderabad, Hyderabad 500 046, India
email: sdgsp@uohyd.ernet.in

MS received 23 February 1998

Abstract. We study third harmonic generation in layered configuration when the fundamental exhibits bistable response. We consider two geometries, namely, a Fabry–Perot cavity with reflection coatings and a distributed feedback structure with alternate nonlinear layers. In both the cases for suitable choice of frequency, the power response at the fundamental frequency is bistable. We show that bistability of the fundamental leads to a multivalued character of the generated third harmonic in both the forward and backward directions. Moreover, we study frequency response in the case of the Fabry–Perot cavity and show that additional structures arise in the generated third harmonic due to frequency bistability of the fundamental. Our calculations suggest the possibility of an all optical switch at third harmonic frequency controlled by the parameters (like intensity, frequency) of the fundamental.

Keywords. Layered media; third harmonic generation; optical bistability.

PACS No. 42.65

1. Introduction

Harmonic generation in layered or periodically modulated media has been drawing considerable attention [1–3]. It has been well known that the nonlinear processes in various materials can be enhanced by using suitable geometries. Resonances and the associated local field enhancements have been utilized to lower the threshold for nonlinear processes and increase their efficiency. To this end high quality factor (high Q) modes of a Fabry–Perot cavity or a distributed feedback structure as well as surface and guided modes have been exploited [4–11]. Use of the reflection coatings in Fabry–Perot cavities leads to such high Q modes [10]. In finite distributed feedback structures such modes arise at the edge of the Bragg rejection bands [12, 13]. Optical bistability and multistability using such modes have been theoretically demonstrated [8].

leads to a corresponding enhancement in the generated harmonic. However, in all these studies the bistable behavior of the fundamental which is crucial near a resonance was neglected. Because of large local field enhancement the self action of the fundamental can not be neglected. It is thus necessary to reexamine the harmonic generation process when there is allowance for this self action leading to the bistability of the fundamental. In this paper we study third harmonic generation in cavities supporting high Q-modes where the bistable behavior of the fundamental is taken into account. We consider two types of cavity configurations, namely, Fabry–Perot cavity with reflection coatings and a distributed feedback cavity with alternating linear and nonlinear slabs. We assume that the generation of the third harmonic does not deplete the pump though we include nonlinear response of the fundamental. In other words, third harmonic wave does not affect the fundamental but bears the signature of the bistable response at the fundamental frequency. We show that the third harmonic also shows bistable behavior in the same domain as the fundamental. Our studies suggest that one may possibly devise a switch at the third harmonic frequency which is controlled by the fundamental intensity or frequency. In all our calculations due to lack of dispersion data for the media considered, we were forced to assume the media to be dispersionless. Hence we could not incorporate the phase-matching aspects of harmonic generation. With the availability of dispersion data the periodic structure can be designed to incorporate quasi phase-matching leading to better harmonic output [14, 15].

The organization of the paper is as follows: In § 2 we present the mathematical formulation and recall some of the results pertaining to optical bistability in layered media. In § 3 we present the results of our numerical investigations for both the systems, namely, Fabry–Perot and distributed feedback cavities and in § 4, we conclude the paper.

2. Mathematical formulation

Let us consider a stratified medium consisting of linear and nonlinear slabs with linear refractive indices n_l and n_n and widths d_l and d_n, respectively. As mentioned in the introduction, we assumed the media to be dispersionless though dispersion can be incorporated in a trivial fashion. The nonlinearity is assumed to be cubic in nature. The composite medium is embedded in a linear medium with refractive index n_i. Let z be the direction of propagation for a y-polarized electromagnetic wave at frequency ω, normally incident on the left edge of the system. Since the nonlinear medium is assumed to be isotropic a y-polarized fundamental leads to a nonlinear polarization also along y direction. The total nonlinear polarization induced in a nonlinear slab can be written as

$$P_{3\omega} = \chi^{(3)} (E_{\omega}^{3} + 6|E_{\omega}|^{2} E_{3\omega} + 3|E_{3\omega}|^{2} E_{3\omega}), \tag{3}$$

where E_ω and $E_{3\omega}$ are the electric fields at the fundamental and generated third harmonic frequencies, respectively. In writing eq. (1) we ignored the frequency dependence of $\chi^{(3)}$. We also ignore the effects of higher order harmonics. Henceforth we neglect the effect of third harmonic on the fundamental assuming $|E_{3\omega}| \ll |E_\omega|$. Hence the propagation equations for the fundamental inside the nonlinear slab becomes

$$\frac{\mathrm{d}^2 \tilde{E}_\omega}{\mathrm{d}\tilde{z}^2} + n_n^2 \tilde{E}_\omega = -3|\tilde{E}_\omega|^2 \tilde{E}_\omega, \tag{4}$$

where, we have introduced the dimensionless quantities: $\tilde{z} = k_0 z$ and $\tilde{E}_\omega = \sqrt{4\pi\chi^{(3)}} E_\omega$. As mentioned earlier, in eq. (4) we retained only the term leading to bistability which is crucial near resonance. The equations at 3ω can be written as

$$\frac{\mathrm{d}\tilde{E}_{3\omega}}{\mathrm{d}\tilde{z}} = 3i(-\tilde{H}_{3\omega}), \tag{5}$$

$$\frac{\mathrm{d}(-\tilde{H}_{3\omega})}{\mathrm{d}\tilde{z}} = 3i[n_n^2 \tilde{E}_{3\omega} + \tilde{E}_\omega^3 + 3|\tilde{E}_{3\omega}|^2 \tilde{E}_{3\omega} + 6|\tilde{E}_\omega|^2 \tilde{E}_{3\omega}], \tag{6}$$

where $\tilde{E}_{3\omega} = \sqrt{4\pi\chi^{(3)}} E_{3\omega}$. A similar scaling has been used for $\tilde{H}_{3\omega}$.

In what follows, we recall the transfer matrix method used to study the propagation characteristics of the fundamental for linear and nonlinear media. For a linear layer the corresponding characteristic matrix is well known [16]. The tangential components of the electric and magnetic fields, at the right and left of the linear slab, at any frequency can be related by means of this characteristic matrix. As we have neglected the effect of dispersion in our system, the structure of this transfer matrix assumes the same form (except for the wave vector) for both the fundamental as well as the third harmonic. The propagation characteristics of the fundamental and the third harmonic inside a nonlinear slab are studied separately. As far as the fundamental is concerned the nonlinear transfer matrix method is applied [10]. Here we recall only the essential steps. The characteristic matrix of the nonlinear slab depends on the intensities of the forward and backward waves in that medium. The solutions of the fundamental wave equation (eq. (4)) for any jth nonlinear slab can be written as [5, 10]

$$\tilde{E}_{\omega j} = A_{+j}\, \mathrm{e}^{i n_{+j} \tilde{z}} + A_{-j}\, \mathrm{e}^{-i n_{-j} \tilde{z}}, \tag{7}$$

where A_{+j} and A_{-j} are the forward and backward wave amplitudes respectively and n_{+j} and n_{-j} are defined as

$$(n_{+j}+n_{-j})\left\lfloor -n_{+j}n_{-j}(\mathrm{e}^{in_{+j}d_n}-\mathrm{e}^{-in_{-j}d_n}) \quad n_{+j}\,\mathrm{e}^{in_{+j}d_n}+n_{-j}\,\mathrm{e}^{-in_{-j}d_n}\right\rfloor$$

The knowledge of the fundamental in the nonlinear slab is used to evaluate the source terms in eqs (5) and (6). The propagation equations for the third harmonic (eqs (5) and 6)) are solved numerically after the distribution of the fundamental in the layers is obtained. From the knowledge of the tangential components of the generated third harmonic at the right edge of any jth nonlinear slab one can obtain the components at the left edge by numerically integrating eqs (5) and (6) along the length of the slab.

We start our calculations from the right end of the whole system. We treat the transmitted fundamental amplitude as a parameter. For a given value of the transmitted fundamental amplitude we propagate the fundamental wave from right to left by using the characteristic matrix for linear and nonlinear slabs. The total characteristic matrix, M, for the entire system is written in terms of the characteristic matrices of each layer. Then the incident (A_{in}) and reflected (A_{r}) amplitudes of the fundamental wave in the medium of incidence can be written in terms of amplitude (A_{t}) of the medium in which the wave is transmitted as follows

$$\begin{pmatrix} A_{\text{in}} \\ A_{\text{r}} \end{pmatrix} = \frac{1}{2n_i}\begin{pmatrix} n_i & 1 \\ n_i & -1 \end{pmatrix} M \begin{pmatrix} 1 \\ n_i \end{pmatrix} A_{\text{t}}. \tag{10}$$

The transmission coefficient for the composite medium at fundamental frequency is given in terms of the elements, m_{ij} of M as

$$T = \left| \frac{2n_i}{(m_{11}+m_{12}n_i)n_i + (m_{21}+m_{22}n_i)} \right|^2. \tag{11}$$

In the case of the third harmonic our calculation starts with a guessed value of transmitted third harmonic amplitude at any transmitted fundamental amplitude. As we did in the case of fundamental, we propagate back the third harmonic wave by calculating the field components at each interface of the system. In the case of linear slabs characteristic matrix approach and for nonlinear slabs the corresponding numerical solutions are used. We then express the incident and reflected third harmonic amplitudes in the medium of incidence in terms of this guessed value of transmitted amplitude. As there is no incident third harmonic, we obtain an expression of the form

$$\tilde{A}_{\text{in}} = f(\tilde{A}_{\text{t}}, A_{\text{t}}, \omega) = 0, \tag{12}$$

where $\tilde{A}_{\text{in}}(\tilde{A}_{\text{t}})$ is the incident (transmitted) third harmonic. Equation (12) is solved for $\tilde{A}_{\text{t}}$ for a given A_{t} which leads to an unique A_{in}. Thus, the solution of eq. (12) leads to the generated transmitted ($\tilde{A}_{\text{t}}$) and reflected ($\tilde{A}_{\text{r}}$) for null input at 3ω.

It was mentioned in the introduction that one has to have cavities supporting high-Q modes in order to have low-threshold nonlinear optical phenomena. We have considered

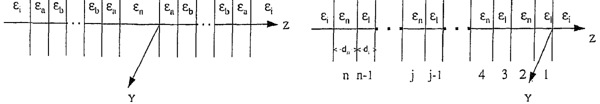

Figure 1. Schematic view of (**a**) Fabry–Perot cavity with reflection coatings with medium parameters $\varepsilon_a = 5.29$, $\varepsilon_b = 1.71$, $\varepsilon_n = 2.5408$ and $\varepsilon_i = 1$ and (**b**) distributed feedback structure with alternating linear and nonlinear slabs with medium parameters $\varepsilon_l = 1.71$, $\varepsilon_n = 2.5408$, $\varepsilon_i = 1$, $d_l = 0.25\lambda$ and $n = 2m = 40$.

2.1 *Fabry–Perot cavity with reflection coatings*

It is well understood that the airy resonances of a Fabry–Perot cavity can be made narrower by increasing the mirror reflectivities. Here we study a composite medium (see figure1a) with one nonlinear slab of linear dielectric constant ε_n, coated on both sides by alternating m low-index (ε_b) and $m+1$ high-index (ε_a) $\lambda/4$ slabs. The initial and final media are linear with the same material of dielectric constants ε_i.

For any transmitted fundamental amplitude (A_t) the forward (A_+) and backward (A_-) amplitudes inside the nonlinear slab can be written as

$$\begin{pmatrix} A_+ \\ A_- \end{pmatrix} = \frac{1}{n_+ + n_-} \begin{pmatrix} n_- & 1 \\ n_+ & -1 \end{pmatrix} M_l \begin{pmatrix} 1 \\ n_i \end{pmatrix} A_t, \tag{13}$$

where M_l is the linear characteristic matrix for the reflection coatings [10]. The above coupled equations along with eq. (8) are solved by using fixed point iteration method to obtain the characteristic matrix M_n of eq. (9). The total characteristic matrix M is then calculated as $M_l M_n M_l$ for the entire system. Using eq. (10) one can then obtain the incident amplitude (A_{in}) and the transmission coefficient T at the fundamental frequency.

For a guessed value of third harmonic amplitude ($\tilde{A}_t$) at the medium of transmittance, the third harmonic tangential field components at the right edge of the nonlinear slab can be written as

$$\begin{pmatrix} \tilde{E}_{3\omega} \\ -\tilde{H}_{3\omega} \end{pmatrix}_{z=0} = M_l \begin{pmatrix} 1 \\ n_i \end{pmatrix} \tilde{A}_t. \tag{14}$$

We integrate the propagation eqs (5) and (6) along the width d_n of the nonlinear slab making use of the knowledge of the distribution of the fundamental amplitudes in order to get the field components at $z = -d_n$. Then the third harmonic incident ($\tilde{A}_{\text{in}}$) and reflected ($\tilde{A}_r$) amplitudes in terms of $\tilde{A}_t$ is written as

$$\begin{pmatrix} A_{j+} \\ A_{j-} \end{pmatrix} = \frac{1}{n_{j+} + n_{j-}} \begin{pmatrix} n_{j-} & 1 \\ n_{j+} & -1 \end{pmatrix} M_{j-1} M_{j-2} \cdots M_1 \begin{pmatrix} 1 \\ n_i \end{pmatrix} A_t, \tag{16}$$

for any transmitted fundamental amplitude A_t which yields the characteristic matrix M_j at fundamental frequency for the jth layer. Thus the total characteristic matrix M for the entire system at fundamental frequency can be obtained as $M_n M_{n-1} M_{n-2} \cdots M$ where $n = 2m$ is the total number of layers. Once M is calculated for the entire system the amplitudes in the layer of incidence and the transmission coefficient are obtained as in the case of Fabry–Perot cavity as explained in the previous section.

In the case of the generated third harmonic wave we propagate the field amplitudes from one period as outlined earlier. In each nonlinear medium we use the corresponding fundamental amplitude while solving the propagation equations. Thus the third harmonic incident ($\tilde{A}_{\text{in}}$) and reflected ($\tilde{A}_r$) amplitudes in the medium of incidence is written for any guessed value of the total transmitted third harmonic amplitude ($\tilde{A}_t$) as

$$\begin{pmatrix} \tilde{A}_{\text{in}} \\ \tilde{A}_t \end{pmatrix} = \frac{1}{2n_i} \begin{pmatrix} n_i & 1 \\ n_i & -1 \end{pmatrix} \begin{pmatrix} \tilde{E}_n \\ -\tilde{H}_n \end{pmatrix}, \tag{17}$$

where $\tilde{E}_n$ and $\tilde{H}_n$ are the tangential components at the left edge of the nth layer. As we have explained before the roots of the above equation with the condition $\tilde{A}_{\text{in}} = 0$ gives the generated third harmonic reflected and transmitted amplitudes.

3. Numerical results and discussion

In this section we present the results of our numerical investigation separately for the cases of Fabry–Perot and distributed feedback cavities.

3.1 *Fabry–Perot cavity with reflection coatings*

In the case of the Fabry–Perot cavity we have chosen the system parameters as, $\varepsilon_n = 2.5408$, $\varepsilon_a = 5.29$ and $\varepsilon_b = 1.71$. The initial and final media are considered to be vacuum with $\varepsilon_i = 1$. The optical width of the nonlinear medium is taken to be $k_0 d_n \sqrt{\varepsilon_n} = 2(1 - \Delta)\pi$ where $\Delta = 0.018$ is the dimensionless resonance half-width. We have chosen the operating point in such a way that the system is detuned slightly by an amount $-2\Delta\pi$ from the peak position of the resonance. In figure 2 we have reproduced the bistability

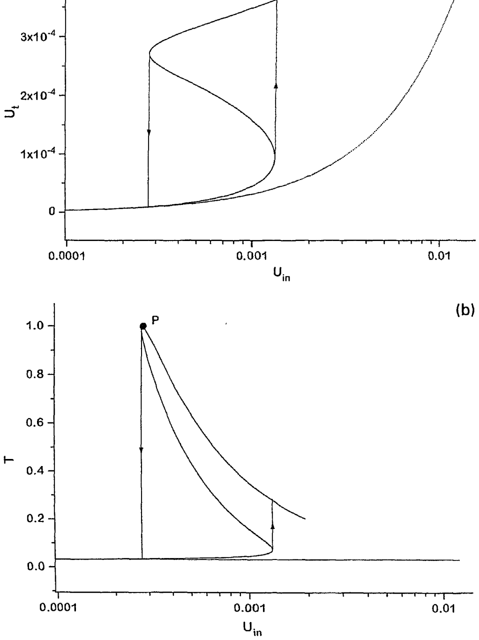

Figure 2. Fundamental (**a**) transmitted intensity U_{t} and (**b**) transmission coefficient T as functions of fundamental incident intensity U_{in} for $k_0 d_n \sqrt{\varepsilon_n} = 2\,(1 - \Delta)\pi$ with $\Delta = 0.018$. Solid (dotted) curve is with (without) self action of the fundamental. The other parameters are as in figure 1a.

features at the fundamental frequency. In figure 2a, b we have plotted transmitted fundamental intensity, $U_{\mathrm{t}} = |A_{\mathrm{t}}|^2(T)$ as a function of incident fundamental intensity, $U_{\mathrm{in}} = |A_{\mathrm{in}}|^2$. The dotted curve in figures 2a and 2b shows the linear behavior of the system

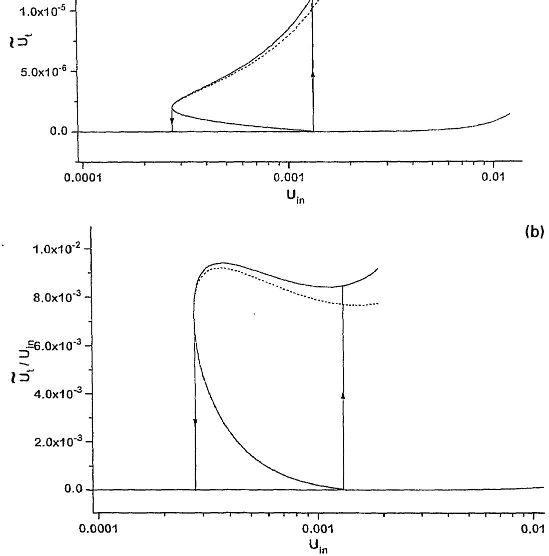

Figure 3. (**a**) Third harmonic transmitted intensity $\tilde{U}_{\rm t}$ and (**b**) $\tilde{U}_{\rm t}/U_{\rm in}$ as functions of $U_{\rm in}$. Solid (dotted) is with (without) self action at ω. The dashed curve gives the result when self action at 3ω is ignored. The parameters of the cavity are as in figure 2.

dotted curve shows the third harmonic output when nonlinear response of fundamental is ignored. The dashed curve explains the system behavior where we have neglected the self action terms of the third harmonic in the propagation equation (i.e., $3|\tilde{E}_{3\omega}|^2\tilde{E}_{3\omega}$ in eq. (6)). It is clear from the curve that the self action effects at 3ω are prominent only for higher values of incident fundamental intensity. Figure 3b shows the dependence of $\tilde{U}_{\rm t}/\tilde{U}_{\rm in}$ as function of $U_{\rm in}$. It is clear from figures 2 and 3 that generated third harmonic can be switched from low to high (high to low) values simply by changing the fundamental intensity. Thus one can have an efficient switch at third harmonic frequency which is

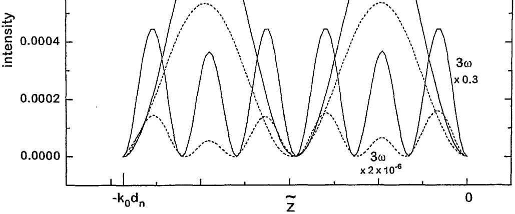

Figure 4. Intensity distribution along the length of the nonlinear slab of the Fabry–Perot cavity of figure 1a where electric field intensities at ω and 3ω are plotted as a function of $\tilde{z}$. The solid (dashed) curve gives our (Bethune's) results. Various curves are labeled by their corresponding frequencies. Note also the different scale factors for various curves.

In order to have a better understanding of the harmonic generation process and to make contact with Bethune's approach we study the field distribution at fundamental and third harmonic frequencies along the length of the nonlinear material. Note that Bethune's results can be recovered from our general results by setting the right hand side of eq. (4) to zero. In other words when there is no self action of the fundamental we have standard plane standing waves at the fundamental frequency the distribution of which determines the generated third harmonic. The results corresponding to the peak of the transmission (see point P in figure 2b which corresponds to $k_0 d_n = 3.8708$, $U_{\text{in}} = 2.7402 \times 10^{-4}$, $U_{\text{t}} = 2.71 \times 10^{-4}$) are shown in figure 4. The solid (dashed) curves give the results for our (Bethune's) approach. We have plotted the electric field intensity $|E(\tilde{z})|^2$ as a function of $\tilde{z}$. Various curves are labeled by the corresponding frequency. Note also the scale factor for the third harmonic. It is clear from figure 4 that there can be drastic differences between our results and those where bistable effects at fundamental are ignored. In fact, the value of $k_0 d_n = 3.8708$ corresponds to an operating point which is away from the linear resonance at the fundamental frequency. Thus one has a low transmission, namely $U_{\text{t}} = 9.71 \times 10^{-6}$ for the same value of U_{in} (see the dotted curve in figure 4). As a consequence the field distribution ignoring the bistable effects is much weaker compared to the case where we allow for the nonlinear resonance. The fundamental distribution gets reflected in the strength of the generated third harmonic. One gets a much stronger third harmonic when such nonlinear resonances are taken into account. It is thus clear that while operating near high-Q modes one has to exercise great care and take into account the self action of the wave which can lead to an altogether different result.

We now turn to the frequency response for a fixed fundamental input. The frequency

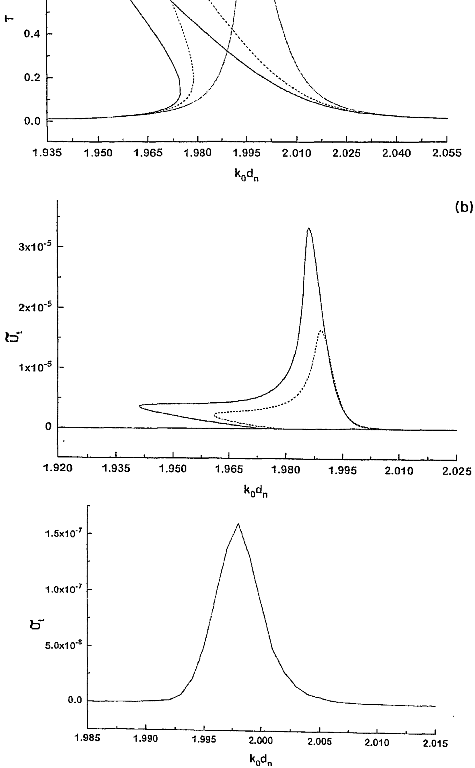

Figure 5. (**a**) Fundamental transmission T and (**b**) transmitted third harmonic intensity $\tilde{U}_t$ for a Fabry–Perot cavity as functions of k_0d_n for three different values U_{I}

$U_i = 3 \times 10^{-5}$ is very small, the dotted curve appears almost flat compared to other curves in figure 5b. Inset to figure 5b shows this output with a different vertical scale. It is clear from figure 5b that for low fundamental input intensities the response at 3ω does not exhibit bistability (see inset to figure 5b). The situation is different when the input is raised to higher values. The response now becomes multivalued depending on the frequency of the fundamental. Moreover, there is a shift of the resonance locations towards left with an increase in the fundamental input. Note that again we have control over the third harmonic intensity by manipulating the fundamental characteristics like frequency.

3.2 *Distributed feedback cavity*

In the case of distributed feedback cavity we considered the superlattice structure consisting of $m = 20$ periods with vacuum on both sides. The values of ε_n and ε_l are 2.5408 and 1.71, respectively. The thickness of each linear slab is taken to be 0.25λ. Figure 6 shows the linear transmission curve at ω for the system and it shows sharp resonances at the edges of the Bragg band. One is likely to obtain enhanced nonlinear effects making use of these resonances. For further analysis we have chosen the operating point close to one of these resonances (see the point R in figure 6) where the optical thickness of each nonlinear slab is taken to be $k_0 d_n \sqrt{\varepsilon_n} = 1.391\pi$. Figure 7a, b shows the bistable response for the fundamental (third harmonic) as functions of incident

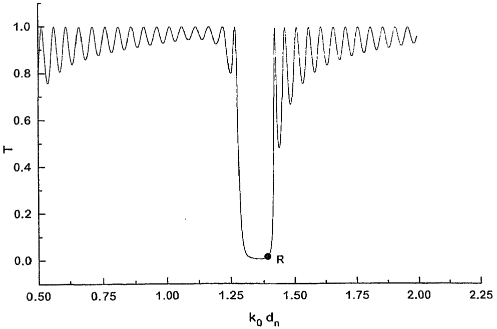

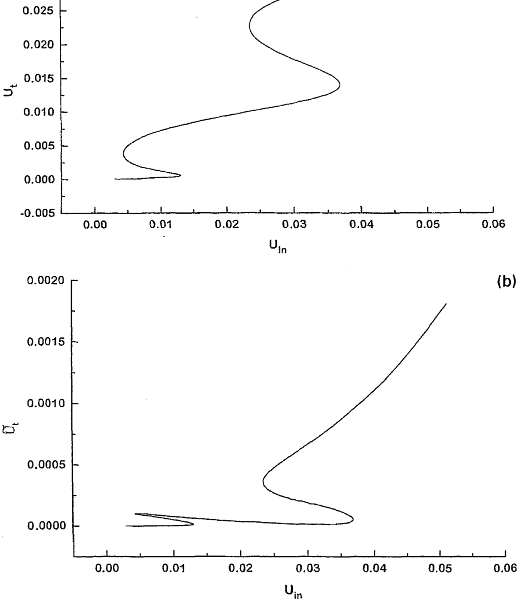

Figure 7. (**a**) U_t and (**b**) $\tilde{U}_\mathrm{t}$ as functions of U_in for a distributed feedback cavity for $k_0 d_n \sqrt{\varepsilon_n} = 1.391\pi$. The other parameters are as in figure 1b.

fundamental intensity. It can be seen from figure 7 that the features observed for the Fabry–Perot cavity are repeated here.

In both the above cases of Fabry–Perot and distributed feedback cavities we also looked at the reflected fundamental wave as well as the generated third harmonic in the backward direction. They also exhibit bistable response as functions of fundamental intensity and frequency. We do not show those results here.

the generated third harmonic. Our calculations suggest the possibility of an all opti switch at third harmonic frequency where the fundamental plays the role of the control fact, fundamental intensity or its frequency can be used to switch the value of generated third harmonic.

Acknowledgements

One of the authors (SDG) would like to thank the Department of Science and Technolo Government of India for support. The authors are also thankful to V Mahalakshmi help in computation.

References

[1] N Bloembergen and P S Pershan, *Phys. Rev.* **128**, 606 (1962)
[2] D S Bethune, *J. Opt. Soc. Am.* **B6**, 910 (1989)
[3] D S Bethune, *J. Opt. Soc. Am.* **B8**, 367 (1991)
N Hashizume, M Ohashi, T Kondo and R Ito, *J. Opt. Soc. Am.* **B12**, 1894 (1995)
[4] D Sarid, *Phys. Rev. Lett.* **47**, 1927 (1981)
S Sarid, R T Deck, A E Craig, R K Hickernell, R S Jameson and J J Fasano, *Appl. Opt.* 3993 (1982)
G S Agarwal, *Phys. Rev.* **B31**, 3534 (1985)
[5] F S Felber and J H Marburger, *Appl. Phys. Lett.* **28**, 731 (1976)
J H Marburger and F S Felber, *Phys. Rev.* **A17**, 335 (1978)
[6] G S Agarwal and S Dutta Gupta, *Phys. Rev.* **B34**, 5239 (1986)
[7] G S Agarwal and S Dutta Gupta, *Opt. Lett.* **12**, 829 (1987)
[8] S Dutta Gupta, *J. Opt. Soc. Am.* **B6**, 1927 (1989)
[9] M B Pande, Ranjit Singh and S Dutta Gupta, *J. Mod. Opt.* **40**, 901 (1993)
[10] S Dutta Gupta and G S Agarwal, *J. Opt. Soc. Am.* **B4**, 691 (1987)
[11] V Mahalakshmi, Jolly Jose and S Dutta Gupta, *Pramana – J. Phys.* **47**, 317 (1996)
[12] P Yeh (ed.), *Optical waves in layered media* (Wiley, New York, 1988) p. 118
[13] S Dutta Gupta and G S Agarwal, *Opt. Commun.* **103**, 122 (1993)
[14] The concept and implementation of quasi phase matching was developed keeping in v mostly second order nonlinear processes. See, for example, J A Armstrong, N Bloemberg J Ducuing and P S Pershan, *Phys. Rev.* **127**, 1918 (1962)
J D Bierlein, *Guided wave optics* edited by D B Ostrowsky and R Reinisch (Klu Academic, Dordrecht, 1992) p. 49
M M Fejer, *Guided wave optics* edited by D B Ostrowsky and R Reinisch (Kluwer Academ Dordrecht, 1992) p. 133
M M Fejer, G A Magel, D H Jundt and R L Byer, *IEEE J. Quantum Electron.* **28**, 2631 (19
[15] D Williams, D West and T King, presented at the European Quantum Electronics Conferen September 8–13 (Hamburg, Germany, 1996)
[16] M Born and E Wolf, *Principles of optics* (Macmillan, New York, 1965) p. 62

Generation of squeezed atomic states in cavity QED

ADITI RAY and R R PURI
Theoretical Physics Division, Central Complex, Bhabha Atomic Research Centre,
Mumbai 400 085, India
Email: krsrini@magnum.barct.ernet.in

MS received 8 July 1997; revised 31 October 1997

Abstract. A squeezed atomic state is that state of a system of two-level atoms for which the intrinsic quantum noise in a process of measurement is less than the minimum noise obtained by using a spin coherent state. It is shown that such a state is generated in certain time intervals when a non-squeezed atomic state evolves on interaction with a single mode coherent field inside a lossless cavity. The atoms are assumed to undergo one-photon or two-photon transitions between the given two levels. The maximum atomic squeezing is found as a function of the number of atoms and the field strength. The effect of the field-dependent Stark shift is investigated in the case of the atoms undergoing two-photon transitions.

Keywords. Atomic squeezing; coherent state; Stark shift; quantum noise; uncertainty relation.

PACS Nos 42.50; 03.65

1. Introduction

A squeezed state of the electromagnetic (e.m.) field is useful in achieving sub-quantum noise in a process of measurement. In the same way, one expects to achieve sub-quantum noise in a process of measurement involving spins or equivalently atoms by use of particular kind of states which may be called squeezed spin or squeezed atomic states in analogy with the case of the e.m. field. Of particular interest to us here are the measurement processes involving two-level atoms. Clearly, because of their usefulness as a means of reducing quantum noise, the methods of generation of such states are of particular interest. In this paper we propose the methods of generation of squeezed states of two-level atoms in cavity QED. Since a system of two-level atoms is mathematically equivalent to a system of spin-$1/2s$, we will use the terms atoms and spins interchangeably.

The method described here is in terms of a system of two-level atoms interacting with a single e.m. mode in a lossless cavity. We consider two cases of atomic transition. One is when the transition between the levels is by means of absorption or emission of one photon and the other is when that process is mediated by two photons at a time. Those processes are described by the one-photon or two-photon Jaynes–Cummings hamiltonian as the case may be. In each case we determine the maximum attainable squeezing as a

The paper is organized as follows. In § 2 we review the concept of spin squeezing. In § 3 we introduce the model hamiltonians used for generating the squeezed atomic states and present the numerical results. The discussion of the results and the conclusions are presented in § 4.

2. The atomic squeezing

Recall that the product of the variances in two quadrature components of the e.m. field is bound from below by the uncertainty relation and that in the coherent state the uncertainty relation is satisfied with equality with equal variance in the two quadratures. The variance in each quadrature component in the coherent state is $1/2$ (with $\hbar = 1$). A quadrature component is said to be squeezed if its variance is less than its value of $1/2$ obtained in the coherent state. The state in which a quadrature component is squeezed is called a squeezed state of the field. The usefulness of squeezing arises from the fact that a process of measurement carried with a squeezed field will have noise which is less than what is obtained by using the coherent state. The noise obtained by the use of coherent state is the so called standard quantum noise.

A straightforward generalization of squeezing in the e.m. field based on the uncertainty relation leads to the usual definition of squeezing of a system of spins according to which a system of spins is squeezed if the variance in a component of spin is less than half the absolute value of the average of a component orthogonal to it. That definition, however, is ambiguous as it identifies even some spin coherent states as squeezed [1, 2]. Also, it does not reflect any quantum correlations between the spins which is the spirit of the field squeezing [2]. Moreover, in contrast with the case of the e.m. field, a spin system squeezed according to the aforementioned definition does not necessarily lead to a reduction in the quantum noise over what is obtained with a spin coherent state in a measurement process.

Alternative approaches to spin squeezing have therefore been advocated. One approach, due to Kitagawa and Ueda [2], proposes the spin-spin correlations as a measure of spin squeezing. The requirement of reduction in the quantum noise in a measurement involving spins forms the basis of another approach [3]. The spectroscopic measurements with an ensemble of two-level atoms [3] and the fermionic and optical interferometers [4, 5] are some examples of the measurement processes involving spins. Because of their importance in the measurement process, we term those spin states as squeezed which are squeezed in the sense of the quantum measurement theory as explained below.

The measure of quantum noise in a process of measurement involving spins is the parameter [3–6]

$$\xi = N\Delta S_i^2/\langle S_i^{\perp}\rangle^2, \tag{1}$$

state of spins is said to be squeezed if ξ in that state is less than $\xi_{\text{min., coh.}}$ i.e. if

$$\xi < 1. \tag{3}$$

The sensitivity of measurement with a squeezed spin state is thus more than what is obtained with a spin coherent state. With an appropriate choice of a squeezed spin state it can be made to approach $1/N$ [3–7]. Since any pure state of a single spin-$1/2$ is a coherent state it follows that $\xi = 1$ for any pure state of a spin-$1/2$. For a mixed spin-$1/2$ state $\xi > 1$. Thus no state of a system of single spin-$1/2$ is squeezed. It is the quantum nature of the correlations between the spins that characterizes spin squeezing. The meaning and; for certain states; the proof of quantum nature of the correlations is discussed in ref. [7].

In the next section we discuss the possibility of generation of squeezed atomic states in cavity QED by starting from a non-squeezed atomic and the coherent field state.

3. Generation of squeezed atomic states

The states satisfying (3) can be generated by means of a hamiltonian non-linear in spin operators [2, 3]. A way of realizing such a hamiltonian in dissipative cavity QED is proposed in [8]. It is shown there that a system of two-level atoms interacting off-resonance with a low-Q cavity can be described; on adiabatic elimination of the field; in terms of a hamiltonian which is non-linear in atomic i.e. spin operators. The states satisfying (3) are generated also in the interaction of spins with a squeezed reservoir [9, 10]. The method proposed in [3] for generating the squeezed spin states considers two types of hamiltonians. One is the Jaynes–Cummings (JC) type hamiltonian

$$H_{\mathrm{I}} = g_1(a^{\dagger}S_- + S_+a), \tag{4}$$

and the other is

$$H = G(S_+a^{\dagger} + aS_-), \tag{5}$$

where $S_{\pm}$ ($a^{\dagger}, a$) are the collective spin (harmonic oscillator) raising/lowering operators. The hamiltonian (4) arises in many other physical situations. However, the 'anti-resonant' hamiltonian (5) is not of frequent occurrence. For its origin, see [3].

It is shown in [3] that if the harmonic oscillator is prepared initially in the squeezed state then on interaction with the spins according to the hamiltonian (4), squeezing is transferred to the atomic system in certain time intervals. However, an initial coherent state of the h.o. does not squeeze an initially unexcited atomic system if the field is weak i.e. if the average number of photons in the field is very small. The reason for the absence of squeezing in that case is that in a weak field the change in the atomic population oscillators so coupled cannot generate a squeezed state from a coherent state. That fact is brought out also by the explicit analytic expression given in [3] for the atoms interacting with a harmonic oscillator.

In this work we point out the usefulness of a system of current experimental and theoretical interest; namely; the system of N two-level Rydberg atoms interacting with a single-mode field inside a lossless cavity; in generating a squeezed atomic state. Such a system is adequately described in the frame rotating with the field frequency by the JC hamiltonian (4) if each atom undergoes resonant single-photon transitions between its levels. The operators $a, a^\dagger$ in that case are the cavity field annihilation/creation operators. It has been shown in [3] that the spins evolving according to (4) are squeezed in certain time intervals if the h.o. described by $a, a^\dagger$ is prepared initially in a squeezed state. We, however, investigate the squeezing in an initially coherent state field as that is obviously a more convenient choice for the initial field state. The cavity field in that case is known to evolve to a squeezed state in certain time intervals. The correlations in the squeezed field state may be expected to give rise to correlations in the atoms interacting with it. It is indeed confirmed by computation that the atomic state gets squeezed in the same time intervals as the field. We examine the squeezing properties also when the atom-field interaction is mediated by resonant two-photon exchange. The system then is described, in the rotating frame, by the effective two-level hamiltonian [11]

$$H_{\mathrm{II}} = \beta a^\dagger a S_z + g_2(a^{\dagger 2} S_- + S_+ a^2), \tag{6}$$

where g_2 is the two-photon atom-field coupling constant and β determines the field dependent Stark shift. The Stark shift arises due to virtual transitions to the intermediate level eliminated adiabatically to arrive at the effective two-level description. It may be mentioned that the derivation of the effective two-level hamiltonian from the three-level one as given in [11] is applicable to any number of collectively interacting atoms although the system treated in [11] consists of a single atom. The derivation of the effective hamiltonian given in [3] does not use any of the special single atom properties.

The hamiltonians H_{I} and H_{II} commute with $M_{\mathrm{I}} = a^\dagger a + S_z$ and $M_{\mathrm{II}} = a^\dagger a + 2S_z$ respectively. A convenient basis for the states in the Hilbert space of H_{I} (H_{II}) is, therefore, constituted by the states $|m, N_{\mathrm{I}} - m\rangle$ ($|m, (N_{\mathrm{II}} - m)\rangle/2$) where N_{I} (N_{II}) is the eigenvalue of M_{I} (M_{II}) and $|m, p\rangle$ is an eigenstate of $a^\dagger a$ and S_z respectively with eigenvalues $m = 0, 1, 2 \ldots$ and $p = -N/2, \; -N/2 + 1, \ldots, N/2$. The expansion of the eigenstates $|\psi_\lambda^{\mathrm{I}}(N_{\mathrm{I}})\rangle$ and $|\psi_\lambda^{\mathrm{II}}(N_{\mathrm{II}})\rangle$ of H_{I} and H_{II} in terms of their respective basis leads to the recurrence relations

$$\alpha_{\mathrm{II}}(m) = \sqrt{m(m-1)\left(\frac{N+N_{\mathrm{II}}-m}{2}+1\right)\left(\frac{N-N_{\mathrm{II}}+m}{2}\right)}. \tag{8}$$

The two sets of equations (7) are the matrix equations of dimensions up to $N+1$ depending upon the value of $N_{\mathrm{I}}, N_{\mathrm{II}}$. Here we investigate the time evolution of a state under the influence of H_{I} or H_{II} by expanding the initial state in terms of the states $|\psi^{\mathrm{I}}_{\lambda}(N_{\mathrm{I}})\rangle$ or $|\psi^{\mathrm{II}}_{\lambda}(N_{\mathrm{II}})\rangle$. If the initial state is not an eigenstate of $a^{\dagger}a$ and S_z then such an expansion is a superposition of the states with different values of N_{I} or N_{II}. In what follows we study the time evolution of a coherent state of the field. That state is not an eigenstate of $a^{\dagger}a$. In that case we need to diagonalize up to $N+1$ dimensional matrices which can be done exact analytically only for small values of N. We, therefore, diagonalize the hamiltonians by solving the eigenvalue equations (7) numerically and determine the quantum averages of interest in the standard way. A numerical study of the time evolution of the atomic population governed by the hamiltonian (4) has been carried in [12]. Some approximate analytic properties of the eigenstates and the eigenvalues of (4) are discussed in [13].

In what follows we assume all the atoms to be initially in their excited state and the field in the coherent state $|\alpha\rangle$. First we compute as a function of time the field squeezing parameter

$$S = \tfrac{1}{4}[\langle :(a+a^{\dagger})^2 :\rangle - \langle a+a^{\dagger}\rangle^2], \tag{9}$$

where :: denotes normal ordering. The field is said to be squeezed if $S < 1$. We compute also the atomic squeezing parameter (1) with $S_j \equiv S_x$ and $S_j^{\perp} \equiv S_z$:

$$\xi = N\Delta S_x^2/\langle S_z\rangle^2. \tag{10}$$

The squeezing parameters S and ξ exhibit the usual collapses and revivals behaviour. We find that the field and the atoms are squeezed in certain time intervals which are same for both. We determine ξ_m which is the value of ξ at the first minima in the plot of ξ as a function of time. Note that the first minima is most relevant because it is the short time behaviour which is of practical interest as the cavity and the atomic damping effects can influence the dynamics of the system at longer times making the validity of the JC model questionable.

In the following we discuss the dependence of ξ_m on the number of atoms, the strength of the field and, in the case of two-photon transitions, on the extent of the Stark shift.

3.1 *One-photon transitions*

In figure 1 we show the variation of ξ_m as a function of the number N of atoms

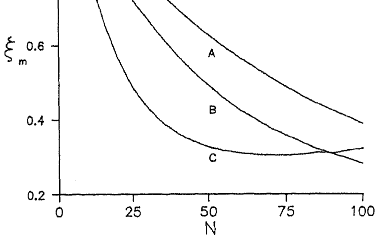

Figure 1. Maximum atomic squeezing ξ_m as a function of the number N of atoms for the atoms undergoing one-photon transitions. The curves A–C are for $|\alpha|^2 = 100$, 64, 25 respectively.

for $|\alpha|^2 = 25$. The position of the minima for other values of α are at much higher values of N.

3.2 *Two-photon transitions*

In the case of two-photon transitions, besides the number of atoms and the field strength, another parameter of interest is the Stark shift parameter β. We investigate the dependence of the maximum squeezing ξ_m on all those parameters by plotting ξ_m as a function of the number N of atoms in a given field for different values of the Stark shift parameter β. In order to compare the squeezing obtainable by using a two-photon process with that obtained in a one-photon process, we select a field value used in figure 1 for one-photon process and investigate the variation of ξ_m as a function of N for different values of the Stark shift in a two-photon process. Thus in figure 2 we plot ξ_m as a function of the number N of atoms for $\alpha^2 = 64$ and for different values $\beta/g_2 = 0, 0.2, 0.5$. That value of α corresponds to the curve B of figure 1. A comparison of figure 2 with curve B of figure 1 shows that the minima in the case of two-photon process shifts to lower values of N as compared to that in one-photon process. A comparison of different curves on figure 2 shows that the squeezing for a given value of N reduces with an increase in the Stark shift.

Next, in order to understand the dependence of ξ_m in the case of two-photon process on the field strength, we plot ξ_m in figure 3 for another value of $\alpha^2 = 100$ which corresponds to curve A of figure 1. A comparison of figure 3 with the curve A figure 1 once again

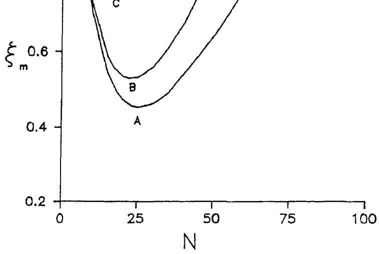

Figure 2. Maximum atomic squeezing ξ_m for $|\alpha|^2 = 64$ as a function of the number N of atoms undergoing two-photon transitions. The curves A–C are for the Stark shift parameter $(\beta/g_2 = 0, 0.2, 0.5)$ respectively.

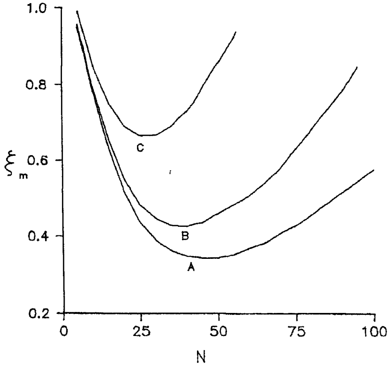

Figure 3. Maximum atomic squeezing ξ_m for $|\alpha|^2 = 100$ as a function of the number N of atoms undergoing two-photon transitions. The curves A–C are for the Stark shift parameter $(\beta/g_2 = 0, 0.2, 0.5)$ respectively.

squeezing reduces with an increase in the Stark shift. The main purpose of figure 3 is,

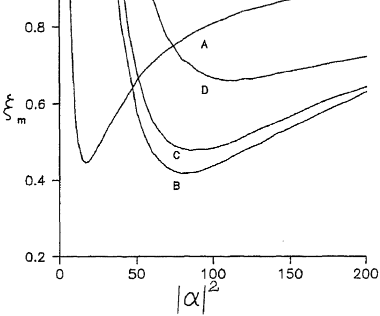

Figure 4. Maximum atomic squeezing ξ_m as a function of $|\alpha|^2$ for $N = 25$. Curve A is for the atoms undergoing single-photon transitions; curves B–D are for the atoms undergoing two-photon transitions with the Stark shift parameter $\beta/g_2 = 0, 0.2, 0.5$ respectively.

value of α for figure 3 is higher than that for figure 2 it follows that the effect of increasing the field strength is in increasing the minimum obtainable squeezing.

Finally, a comparison of ξ_m in one and two photon processes with different Stark shifts is made in figure 4 by plotting ξ_m as a function of the field strength $|\alpha|^2$ for fixed $N = 25$. Curve A is for the atoms undergoing one-photon transitions whereas the curves B–D are for the two-photon process corresponding to the the Stark shift parameter $\beta/g_2 = 0, 0.2, 0.5$ respectively. The Stark shift is found to reduce the squeezing. Also, the minima in ξ_m for a given N occurs at higher $|\alpha|^2$ in a two-photon process as compared with the one-photon process.

4. Discussion and conclusions

The occurrence of minima in ξ_m as a function of the number N of atoms is an interesting and non-trivial feature. That feature can be understood by noting that $\xi_m = 1$ for $N = 1$ and that the state of a collectively interacting system of N two-level atoms is approximately an atomic coherent state at all times if $N \gg 1$ [14]. Hence $\xi_m \simeq 1$ for $N \gg 1$. Since ξ_m is found to decrease as the number of atoms is increased from one it follows that extremum as a function of the field amplitude. Hence, one has to determine the best value of field for maximum squeezing for a given number of atoms. Also, a two-photon process is found to lead to more squeezing as compared with that obtained from a one-photon process for a given value of the number of atoms and the field amplitude. The Stark shift in a two-photon process reduces the attainable squeezing and hence should be minimized.

Finally, it may be remarked that the system discussed here is of current experimental and theoretical interest.

References

[1] K Wodkiewicz and J H Eberly, *J. Opt. Soc. Am.* **B2**, 458 (1985)

[2] M Kitagawa and M Ueda, *Phys. Rev.* **A47**, 5138 (1993)

[3] D J Wineland, J J Bollinger, W M Itano and F L Moore, *Phys. Rev.* **A46**, 6797 (1992)

[4] B Yurke, S L McCall and J R Klauder, *Phys. Rev.* **A33**, 4033 (1986)
B Yurke, *Phys. Rev. Lett.* **56**, 1515 (1986)

[5] M Kitagawa and M Ueda, *Phys. Rev. Lett.* **67**, 1852 (1991)

[6] R R Puri, *Squeezed atomic states and their generation*, Notes of Lectures at SERC School on Coherence and Correlations in Quantum Optics, *Math. Sci.* (1995) and Coherent and Squeezed States on Physical Basis, *Pramana – J. Phys.* **48**, 787 (1997)

[7] R R Puri, *J. Phys.* **A29**, 5719 (1996)

[8] R R Puri and G S Agarwal, *Squeezing in a dispersive cavity* (Paper presented at the International Conference on Squeezed States, Maryland, 1993)

[9] G S Agarwal and R R Puri, *Opt. Commun.* **69**, 267 (1989); *Phys. Rev.* **A41**, 3782 (1990)

[10] G S Agarwal and R R Puri, *Phys. Rev.* **A49**, 4968 (1994)
R R Puri and G S Agarwal, in *Coherent states: past present and future*, edited by J R Klauder and D H Feng (World Scientific, 1994) p. 447

[11] R R Puri and R K Bullough, *J. Opt. Soc. Am.* **B5**, 2021 (1988)

[12] S M Barnett and P L Knight, *Optica Acta* **31**, 435 (1984)

[13] G Scharf, *Helv. Phys. Acta* **43**, 806 (1976)

[14] F Persico and G Vetri, *Phys. Rev.* **A12**, 2083 (1975)
S Kumar and C L Mehta, *Phys. Rev.* **A21**, 1573

Proton NMR in $CeNiInH_{0.53}$ down to liquid helium temperature

R RAY, A GHOSHRAY, K GHOSHRAY and N CHATTERJEE
S.S. and M.P. Division, Saha Institute of Nuclear Physics, 1/AF Bidhan Nagar, Calcutta 700 064, India
Email: agr@cmp.saha.ernet.in

MS received 19 December 1997

Abstract. The NMR probe and the matching network has been designed for the ^1H NMR study in $CeNiInH_{0.53}$ down to liquid helium temperature using Bruker MSL 100 spectrometer. NMR line-shape measurement shows the absence of any signature of proton pairing in $CeNiInH_{0.53}$ down to 3.86 K, as it was observed for high hydrogen concentration. The measurement of the spin-lattice relaxation time in the temperature range 300–20 K reveals that the relaxation rate is mainly governed by the Korringa-type relaxation mechanism.

Keywords. NMR; line shape; spin-lattice relaxation.

PACS Nos 76.60; 76.00

1. Introduction

The evidence of an ordered arrangement of proton pairs with H–H separation ~ 1.5–1.6 Å, as found in Fe_2P type intermetallic hydrides $CeNiInH_x$ and $PrNiInH_x$ $(x \geq 1)$ [1, 2] from NMR, has attracted much interest. Such type of pairing of protons with separation 1.9 Å has recently been observed by Kumitomo *et al* [3] in the sodium insertion compound of hydrogen molybdenum bronze. These results violate Switendick's criterion – the nearest neighbour H–H distance in a metal lattice has never been found to the less than 2.1 Å. However, the discovery of the stable bonding neutral dihydrogen molecules to molybdenum and tungsten complexes by Kubas *et al* [4] has led to the speculation regarding the possibility for two hydrogen atoms in bulk metal hydride to favour either a molecular form of pairing or a pairing of the two hydrogen atoms mediated by a metal atom [5].

In this paper, we report on ^1H NMR studies on $CeNiInH_{0.53}$ in the temperature range 3.8–70 K. Our earlier measurements above 77 K show that in $CeNiInH_x$ with $x < 1.0$, protons do not exist in pairs and they are highly mobile in the interstices. The possibility of pairing of protons as mentioned above even in $CeNiInH_{0.53}$ at low temperatures, wherein hydrogens are supposed to be in rigid condition in comparison with NMR frequency, has led us to do this measurement. Results, however, indicate that there is no such type of pairing of protons in this compound even at liquid helium temperature. Nevertheless, the crystalline sample has been made in subsection 3.1 of § 3 which describes results and discussion.

2. Experimental details

The sample we are using now is the one that we have used earlier. It was kept in a sealed quartz tube filled with argon. We have started the experiment by checking with the NMR and magnetization data and comparing with the earlier data. Magnetization measurement is specially important because, in these samples one can not rule out the possibility of the precipitation of nickel from the hydride. Even a slight precipitation of nickel would act as ferromagnetic impurity.

The relevant physical parameters of $CeNiInH_{0.53}$ which are thought to be essential for clarity of reading, are repeated here. Even after the hydrogenation, the system has been found to be a Fe_2P type compound having a hexagonal closed packed symmetry with $a = 7.57$ Å and $c = 4.01$ Å. Moreover, the effective moment of a magnetic ion, μ_{eff}, in terms of Bohr magneton per formula unit and the paramagnetic Curie temperature θ are close to that of the parent compound CeNiIn which are 1.73 and -57 respectively [6].

2.1 *Construction of NMR probe*

We have constructed a NMR probe for measurements on a solid sample in a continuous flow cryostat for liquid helium. The NMR probe consists of a resonating coil with a suitable matching network for impedance matching of the transmitter and the pre-amplifier. Except the probe assembly we have utilized all other parts of our Bruker MSL 100 spectrometer.

One significant complication when doing NMR in a low temperature environment is the necessity of using a length of coaxial cable (~ 1 m) between the coil and the electronics outside the cryostat. One has two choices; either put the entire tank circuit in the bottom of the cryostat, or include the coax as a part of the tank circuit. The primary advantage of having the entire tank circuit cold is that one can obtain much higher Q's, which can substantially improve the signal to noise for narrow lines. Having the tank in the cryostat forces one to work at a fixed frequency, where both the frequency of operation of the tank and the quality of the match to 50 ohms are likely to change upon cooling down. Single frequency operation is avoidable if one is willing to design into the cryostat the necessary linkage to room temperature that would permit varying the tank tuning while cold. While this can be done it is by no means simple.

The choice of allowing the coax to be included in the tank circuit allows one to vary the frequency of operation: however, analysis of the tank circuit performances is complilike a "magic T" in the front end. The "magic T" takes a signal from the source and splits it into two arms, one of which has a 180° phase shift. One of this arm is connected to the tank circuit (which has to be tuned to 50 Ω); and other to an rf terminator of 50 Ω impedance. Half of the power reflected from the arms is summed and appears at the output. Because of the 180° phase shift, the amount of the drive signal that gets to the output is due to the difference in the power reflected from the tank and from the terminator side. By trimming the condenser one can have a reasonable good match of 50 Ω.

Matching networks. There are ways of changing the impedance of resonant circuits to some desired value. Consider the parallel tank circuit [7] for which the impedance at resonance is $\sim \omega^2 L^2/R = \omega LQ$. The combination of L and C can be chosen at a given frequency to get a desired impedance but sometimes there are constraints which will not allow a free choice of L and thus $L\omega Q$. A common (and easiest to implement) way to transform the impedance of a parallel tank circuit in such cases is to add a series capacitor. The resonance condition is very close to $\omega^2 L(C + C') = 1$, which is a familiar one with C replaced by $C + C'$. The impedance at resonance is still $\omega^2 L^2/R$, as in the parallel tank, but the new L will be smaller than the old by a factor $1 + (C/C')$. Therefore, the new impedance will be smaller than the old by $[1 + (C/C')]^2$.

2.2 *Cryostat*

We have used a top loading continuous flow cryostat CF1200 of Oxford Instruments. A simple arrangement has been made to hold the cryostat in the yoke of Varian's 15″ electromagnet model No. V7400. Provisions are also made to keep the sample portion of the cryostat in a region of maximum homogeneity of the magnetic field. This is generally done by monitoring the intensity of a narrow NMR line. The sample is cooled by conduction through helium gas in the sample space. The flow of liquid which cools the cryostat does not come into direct contact with the sample. The liquid is supplied from a separate storage vessel through an insulated transfer tube; it flows through a heat exchanger around the sample space, and out of the cryostat to the pump. A thermometer and heater are mounted on the heat exchanger and these are used with a temperature controller ITC503 of Oxford Instruments to balance the cooling power of the cryogen and to control the temperature of the heat exchanger. With this arrangement we have been able to maintain a temperature of 3.8 K.

The temperature at the sample site could be monitored by two sensors placed in contact with the NMR coil enclosing the sample. A platinum sensor and a silicon diode sensor were fixed at the two ends of the sample by Apiezon N greeze. There is absolutely no temperature difference between the two ends in the temperature range 20–60 K and this is within ± 0.1 K of the set temperature recorded by the sensor placed in the heat exchanger crystal, results in a characteristic NMR line-shape [8]. This is a consequence of the strong dipolar interaction between the two protons. The Hamiltonian for such a spin pair in a strong applied magnetic field H_0 is given by

$$\mathcal{H} = -\gamma\hbar H_0(I_z^1 + I_z^2) + \frac{\gamma^2\hbar^2}{2r_{12}^3}[3(1-3\cos^2\theta)\, I_z^1 I_z^2 - (1-3\cos^2\theta)\mathbf{I}^1 \cdot \mathbf{I}^2]. \quad (1)$$

Here, θ is the angle between the applied field H_0 and the vector r_{12} joining the two spins. Because of the perturbing term (second part of the Hamiltonian) the resonance line get splitted into two lines. These two resonance lines appear at

$$\nu_\pm = \nu_0 \pm (3\gamma^2 h/16\pi^2 r_{12}^3)(3\cos^2\theta - 1). \quad (2)$$

For a single crystal, the separation of these two resonances from the unperturbed position ν_0 is a function of the angle θ. For a polycrystalline sample, the crystallites are oriented at all possible θ. The intensity pattern for the two transitions can be obtained as

$$I_\pm(\nu') = \int_{-\infty}^{\infty} P(\nu) \exp[-(\nu_\pm - \nu')^2/2\omega^2] \mathrm{d}\nu, \quad (3)$$

where, $P(\nu)$ is the distribution function and is expressed as $P(\nu) \propto \int_0^{2\pi} \int_{-1}^{1} (\mathrm{d}(\cos\theta)/\mathrm{d}\nu)\, \mathrm{d}\phi$, $\exp[-(\nu_\pm - \nu')^2/2\omega^2]$ expresses the component line with ω as the root-mean-square deviation of frequency from the Larmor frequency.

In figure 1, computer generated line-shapes expected from the dipolar interaction between a close pair of protons with different proton–proton spacing (r_{12}) are shown. It is

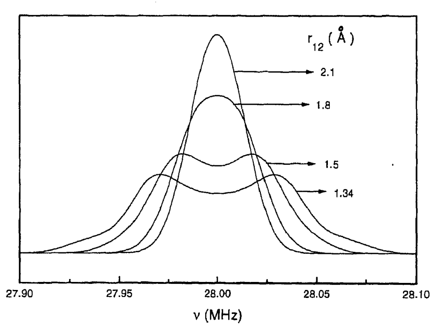

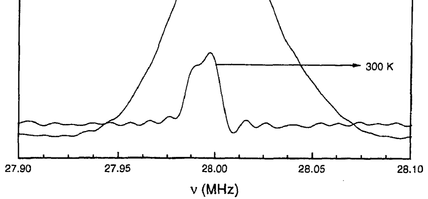

Figure 2. The experimental line-shape of ^{1}H NMR in CeNiInH$_{0.53}$ at 300 K and 6 K. The spectra were obtained at 28 MHz using solid-echo pulse sequence $(90° - \tau - 90°)$.

clear from the figure that when the proton–proton spacing is less than 2.1 Å line-shape shows a characteristic Pake doublet pattern, whereas, if the protons are randomly distributed throughout the interstitial sites the resonance line-shape will not display the doublet-peak structure characteristic of the strong dipolar interaction.

A comparison of the observed proton resonance in CeNiInH$_{0.53}$ at 6 K and 300 K as shown in figure 2, with the theoretically generated line-shape reveals that the ^{1}H–^{1}H separation in CeNiInH$_{0.53}$ is not less than 2.1 Å i.e. the protons in CeNiInH$_{0.53}$ are not in the paired state down to 3.86 K. As the temperature is decreased down to 3.86 K the line-width $(\delta\nu)$ of the NMR line-shape get increased. The temperature variation of $\delta\nu^{-1}$ shows that the line-width of the NMR line-shape is almost governed by the broadening due to susceptibility.

3.2 *Spin-lattice relaxation time*

We consider that the measured spin-lattice relaxation rate T_1^{-1} over the temperature range investigated (300–20 K) arises from three contributions

$$T_1^{-1} = (T_1)_K^{-1} + (T_1)_{RKKY}^{-1} + (T_1)_{d,ce}^{-1} \tag{4}$$

where, $(T_1)_K^{-1}$ is the conduction electron contribution which follows the Korringa relation $(T_1)_K^{-1} = C_K T$. $(T_1)_{d,ce}^{-1}$ is the dipolar coupling of proton to the electronic magnetic moment of each Ce^{3+} ion. $(T_1)_{RKKY}^{-1}$ is due to the interaction between the proton and the localized *f* electron through the conduction electrons.

The ^{1}H spin lattice relaxation time T_1 has been measured at 28 MHz using inversion-recovery $(180° - \tau - 90°)$ technique. The spin-lattice relaxation rate, T_1^{-1} of proton in

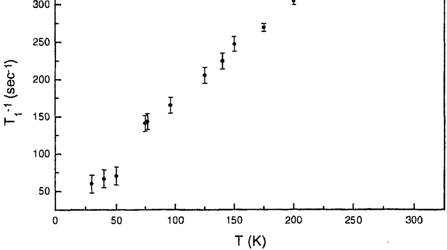

Figure 3. The temperature variation of spin-relaxation rate (T_1^{-1}) of proton in $CeNiInH_{0.53}$ in the temperature range 300–20 K.

decreases linearly with the lowering of temperature. This indicates that in the temperature range 225–20 K the relaxation mechanism is dominated by the Korringa-type relaxation mechanism and there is no effect of any localized magnetic moment. This observation suggests the complete delocalization of $4f$ electron of Ce ion. Here it is to be mentioned that in case of other rare earth ternary intermetallic hydrides such as $CeNiAlH_x$ and $CeCuAlH_x$ [9], the proton spin-lattice relaxation mechanism is dominated by the influence of localized magnetic moment of Ce^{3+} ion through the RKKY interaction mechanism.

4. Conclusion

Protons do not exist in pairs in case of $CeNiInH_{0.53}$ even at 4 K. The spin-lattice relaxation rate (T_1^{-1}) in the temperature range 20–225 K follows Korringa behaviour. This is in sharp contrast with the observation made in $CeNiAlH_x$ and $CeCuAlH_x$, wherein the effect of f-electron dominates the relaxation mechanism.

Acknowlegement

The authors are thankful to B Basak, S Dutta and A Pal, who are the members of liquid helium production team. We wish to express our indebtedness to Saurav Giri and Prof. B Ghosh for several valuable discussions. We also thank A Biswas for his technical assistance.

References

and references therein

[6] Mita Sen, Saurav Giri, K Ghoshray, B Bandyopadhyay, A Ghoshray and N Chatterje *State Commun.* **89**, 327 (1994)

[7] E Fukushima and S B W Roeder, *Experimental Pulse NMR* (Addison–Wesley Pul Company, 1981)

[8] A Abragram, *The principles of nuclear magnetism* (Clarendon, Oxford, 1961)

[9] B Bandyopadhyay, K Ghoshray, A Ghoshray and N Chatterjee, *Phys. Rev.* **B46**, 2912

1. Place of Publication ... Bangalore

2. Periodicity of Publication ... Monthly

3. Printer's Name ... N Mukunda
Indian Academy of Sciences
Bangalore 560 080

4. and 5. Publisher and Editor ... N Mukunda

6. Nationality ... Indian

7. Address ... Indian Academy of Sciences
P. B. No. 8005
Bangalore 560 080

8. Name and Address of the Owner ... Indian Academy of Sciences
Bangalore 560 080

I, N Mukunda, hereby declare that the particulars given above are true to the best of knowledge.

Dated 1st March 1998

N Mukunda
Signature of Publish

Associate Editor

H R Krishnamurthy
Indian Institute of Science, Bangalore

Editorial Board

G S Agarwal, *Physical Research Laboratory, Ahmedabad*
V Balakrishnan, *Indian Institute of Technology, Chennai*
J K Bhattacharjee, *Indian Assoc. for the Cultivation of Science, Calcutta*
D N Bose, *Indian Institute of Technology, Kharagpur*
B M Deb, *Panjab University, Chandigarh*
Rohini M Godbole, *Indian Institute of Science, Bangalore*
S Kailas, *Bhabha Atomic Research Centre, Mumbai*
R K Kaul, *The Institute of Mathematical Sciences, Chennai*
A V Khare, *Institute of Physics, Bhubaneswar*
T Padmanabhan, *Inter Univ. Centre for Astronomy and Astrophysics, Pune*
R Ramaswamy, *Jawaharlal Nehru University, New Delhi*
A K Raychaudhuri, *National Physical Laboratory, New Delhi*
K C Rustagi, *Centre for Advanced Technology, Indore*
E V Sampathkumaran, *Tata Institute of Fundamental Research, Mumbai*
Abhijit Sen, *Institute for Plasma Research, Gandhinagar*
S K Sikka, *Bhabha Atomic Research Centre, Mumbai*
Y Singh, *Banaras Hindu University, Varanasi*

Editor of Publications of the Academy

N Mukunda
Indian Institute of Science, Bangalore

Annual Subscription Rates

All countries except India US$ 200
(Price includes AIR MAIL charges)
India Rs. 200

Annual subscriptions for individuals for India and abroad are Rs. 100/- and $50 respectiv

All correspondence regarding subscription should be addressed to the Circulation Departme
the Academy.

Editorial Office

Indian Academy of Sciences, C V Raman Avenue,
PB No. 8005, Bangalore 560 080, India

Telephone: 334 2546
Telefax: 91-80-334 6094

Email: pramana@ias.ernet.in